

Self-Organization of Iron Sulfide Nanoparticles into Complex Multi-Compartment Supraparticles

*E. SumeYra Turalt-Emre^{1,6}, Ahmet E. Emre^{1,6}, Drew A. Vecchio^{2,6}, Usha Kadiyala^{4,6},
J. Scott VanEpps^{4,5,6*}, and Nicholas A. Kotov^{1,2,3,5,6*}*

¹Biomedical Engineering Department, University of Michigan, Ann Arbor, MI, 48109, USA

²Chemical Engineering Department, University of Michigan, Ann Arbor, MI, 48109, USA

³Materials Science and Engineering Department, University of Michigan Ann Arbor, MI, 48109, USA

⁴Department of Emergency Medicine, University of Michigan, Ann Arbor, MI, 48109, USA

⁵Macromolecular Science and Engineering Department, University of Michigan, Ann Arbor, MI, 48109, USA

⁶Biointerfaces Institute University of Michigan; University of Michigan; Ann Arbor, MI, 48109, USA

Email: jvane@umich.edu; kotov@umich.edu

Keywords: self-assembly, compartmentalization, inorganic nanoparticle, supraparticles, biomimetic particles, cellular organelles, artificial virus

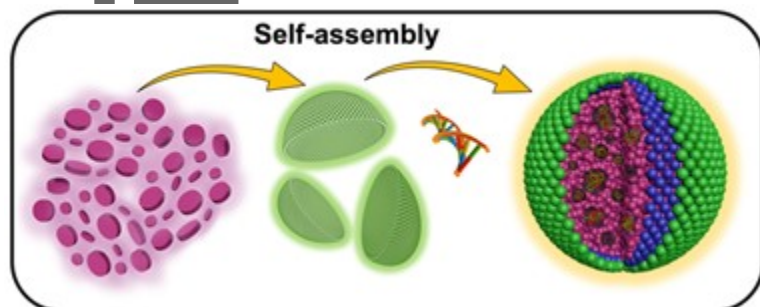
ABSTRACT: Self-assembled compartments from nanoscale components are found in all life forms. Their characteristic dimensions are in 50-1000 nm scale, typically assembled from a variety of bioorganic ‘building blocks’. Among various functions that these mesoscale compartments carry out, protection of the content from the environment is central. Finding synthetic pathways to similarly complex and functional particles from technologically friendly inorganic nanoparticles (NPs) is needed for multitude of biomedical, biochemical, and biotechnological processes. Here, we show that FeS₂ NPs stabilized by *L*-cysteine self-assemble into multicompartment supraparticles (mSPs). The NPs initially produce ~55 nm concave assemblies that reconfigure into ~75 nm closed mSPs with ~340 interconnected compartments with an average size of ~5 nm. The inter-compartmental partitions and mSP surface are formed primarily from FeS₂ and Fe₂O₃ NPs, respectively. The intermediate formation of cup-like particles enables encapsulation of biological cargo. This capability was demonstrated by loading mSPs with DNA and subsequent transfection of mammalian cells. We also found that the temperature stability of the DNA cargo was enhanced compared to the traditional delivery vehicles.

This is the author manuscript accepted for publication and has undergone full peer review but has not been through the copyediting, typesetting, pagination and proofreading process, which may lead to differences between this version and the [Version of Record](#). Please cite this article as [doi: 10.1002/adma.202211244](https://doi.org/10.1002/adma.202211244).

This article is protected by copyright. All rights reserved.

These findings demonstrate that biomimetic compartmentalized particles can be used to successfully encapsulate and enhance temperature stability of nucleic acid cargo for a variety of bioapplications.

Graphical abstract



1. Introduction

Mesoscale compartmentalization with enclosures ranging from ~50 nm to 1,000 nm is one of the key structural motifs in living matter¹⁻⁴ and is observed even in the simplest lifeforms.⁵⁻⁷ Examples of such self-assembled biological structures include various viruses, cellular vesicles,⁸ and numerous organelles exemplified by carboxysomes,⁹ endosomes, and lysosomes.^{4,10} The constitutive biomolecules of these nanoassemblies are diverse - lipids, proteins, oligosaccharides, and polynucleotides - but, interestingly enough, all of them are in nanoscale dimensions.^{4,10,11} Protection of the segregated molecular content from environmental degradation or competitive reactions is the most common function of these assemblies, with additional functions including transport, metabolism, sensing, and signaling. Looking at the intracellular organelles with higher complexity, many of them, such as the endoplasmic reticulum (ER), Golgi apparatus, mitochondria, and chloroplast, have multiple interconnected compartments with numerous functionalities.¹² As such, ER is one of the biggest organelles in eukaryotic cells and is responsible for multiple functionalities such as protein synthesis, folding, modification, lipid/carbohydrate metabolism, and calcium storage. These different functions occur in parallel manner in different structural domains of ER located in close proximity.

Compartmentalization within one organelle makes it possible while avoiding enzymatic degradation, reaction cross-talk, and chemical interference.¹³

Compartmentalization is, therefore, essential for organelle-like nanoassemblies with similar functionalities representing one of the easily identifiable structural targets in engineering biomimetic nanomaterials. Synthetic mesoscale (*ca* 50 nm – 1,000 nm) and microscales (*ca* 1,000-10,000 nm) particles with single or multiple compartments made from organic amphiphilic compounds,^{4,14,15} such as lipids,¹⁶⁻¹⁸ polymers¹⁹ and nucleic acids,^{20,21} that form liposomes,^{22,23} polymersomes^{1,24,25}, capsosomes²⁶⁻²⁸, and protocells^{1,16,29} have been extensively investigated. In contrast, compartmentalized superstructures made from inorganic nanoparticles (NPs) are much less common. Their unique optical,^{30,31} mechanical,³² catalytic, and biological characteristics^{33,34} can expand and facilitate the engineering of the NP-based ‘organelles’ with similar and different functionalities as their prototypes. However, the common methodology of using organic structures as templates and complex multistep processes negates many of these advantages.³⁵⁻³⁷ Toxic solvents and costly biological components also make them environmentally and technologically unfriendly.³⁸⁻⁴³

To address these problems and to develop a generalized scalable approach for their synthesis, one can utilize an intrinsic ability of inorganic NPs to self-assemble⁴⁴. In fact, the self-organization behavior of metals, semiconductors, or ceramic NPs replicates that of nanoscale biological components,⁴⁵⁻⁴⁹ imparting them with the chemical and thermal robustness of inorganic materials. Utilization of NPs with various geometrical symmetries combined with the non-classical crystallization processes,^{47,50} can also expand the variety of possible structures and complex geometries.⁵¹⁻⁵³ However, the prior studies on self-assembly typically lead to nanostructured solids and semi-infinite nanoassemblies, such as chains,^{47,54} sheets,⁵⁵ superlattices,⁵⁶ and ribbons,⁵⁷ rather than to compartmentalized particles of specific dimensions. Recently, self-assembly pathways based on electrostatic self-limitation to terminal assemblies with specific dimensions, such as nanoshells,^{3,58} helices,⁵⁹⁻⁶¹ nanostars,⁶² rings,⁶³ blackberries,⁴⁴ and supraparticles (SPs),⁶⁴⁻⁶⁸ were found. This study explicitly shows the self-

organization of FeS₂ NPs into multicompartiment supraparticle (mSP) that has not been observed before. This type of biomimetic nanoassemblies can encapsulate biological cargo, similar to virus-like nanovectors⁶⁹, exemplified by DNA and being demonstrated in this work by plasmids. Importantly, inorganic NPs are expected to expand the temperature range for stability of such formulations.

2. Results and Discussion

Iron sulfide (FeS₂) is the most abundant mineral on Earth, and the central advantages of FeS₂ NPs include low toxicity, bioavailability, and likely biodegradability.⁷⁰ Keeping biocompatibility in mind, the synthesis approach avoided toxic reagents (*i.e.*, dimethyl sulfoxide and ethylenediamine^{71,72}), high boiling point organic solvents, and long-chain surfactants.⁷¹ We investigate the possibility of a simple method that produces biocompatible FeS₂ NPs in aqueous media that facilitates hydrogen bonding and other forces beneficial to NP self-assembly of diverse self-limited superstructures under ambient conditions.⁴⁹ The choice of amino acid surface ligand, namely *L*-cysteine (Cys), was made to take advantage of fully biocompatible chemistry for the NP synthesis. The low molecular weight of this surface ligand also increases the attractive forces between NPs and the anisotropy of their interactions. Careful selection and optimization of the reaction conditions: precursor concentrations, pH, reaction time, and temperature allowed us to define conditions where FeS₂ NPs self-assemble into compartmentalized, positively charged mSPs within 30 min at room temperature (**Figure 1a-e**). After 30 min, mSPs begin to aggregate (**Figure S1**). This data suggests that the observed superstructures are self-limiting terminal assemblies. We stopped the reaction at the optimum time (30 min) to collect well-dispersed mSPs for their further experiments and characterization.

2.1 Constituent Nanoparticles

The building blocks of self-assembled mSPs are simple inorganic NPs coated with short surface ligands. These constituent NPs are synthesized on ice to prevent their spontaneous self-assembly into mSPs. The as-prepared NPs carrying a layer of *L*-Cys display an electrokinetic zeta-potential of $\zeta =$

+20.5 ± 1.5mV (**Figure S2-NP**) and have a disk-like geometry with a diameter of 4.5±1.6 nm and a height of ~1.5 nm based on TEM (**Figure 1f, g, and n**), STEM (**Figure 2a**), and AFM (**Figure 2b**) data. Further analysis, X-ray diffraction (XRD) gives a weak broad peak for NPs (**Figure S3a**), suggesting limited crystallinity despite faceted shapes.⁷³ Hence, electron diffraction (SAED) analysis (**Figure S3b**) was utilized for phase identification, and it revealed that NPs assembled into mSPs display the crystal structure of FeS₂ (Pnnm and Pa-3 space groups, PDF 37-475 and PDF 06-710, respectively) and Fe₂O₃ (Aba-2 space group ICSD 430557) NPs (**Table S1**). Energy dispersion X-ray spectrometry (EDS) also confirms the presence of oxygen (O) along with iron (Fe) and sulfur (S) in NPs (**Figure S3c**). Since the assembly process occurs at ambient conditions, some NPs oxidized and partially transformed into iron oxide NPs (**Figure 2c-d**). Notably, the chemical changes with the NPs do not prevent efficient self-assembly, which indicates the generality of the self-assembly behavior at the nanoscale. Also, note that the presence of Fe₂O₃ NPs does not decrease and, perhaps, further improves biocompatibility^{69,74,75} of the resulting mSPs.

2.2 Intermediate Structures

After the synthesis of NPs, an increase of their dispersion temperature to 25°C allowed NPs to self-assemble. Within 15 min on the pathway from NPs to mSPs, concave nanoassemblies (**Figure 1c and d**), referred here as nanocups, are observed as an intermediate (**Figure 1h and i**). The oblong mSPs (**Figure 1e**) have a closed external surface, whereas the intermediate nanocups are open, and their geometry can be alternatively described as half-shells.

While the intermediate structure and terminal mSPs can be seen together during synthesis (**Figure 1d and j**), there are no nanocups found in the dispersions of mSPs at the end of the reaction (**Figure 1e**), which points to the assembly process as NP → nanocups → mSPs. In addition, broken pieces of mSPs reveal similar concave geometries (**Figure S4**). The average size of the nanocups is 55.2 ± 23.1 nm with ~5nm thickness (**Figure 1o**), and they contain *ca* 300 NPs. Three-dimensional images obtained by scanning electron microscopy - through the lens detector (SEM-TLD) images (**Figure 2e**) show

that the nanocups have an open rim area and closed bottom (**Figure 2g-h**). High-angle annular dark-field (HAADF) scanning transmission electron microscopy (STEM) mode further supports their 3D geometry. Taking the capability of HAADF to provide enhanced contrast between heavy atoms and light atoms or empty (void) areas, the organization of individual NPs in these concave intermediates (**Figure 2f, arrow**) can be understood in a greater level of detail.

2.3 Characterization of Multicompartment Supraparticles

Based on TEM images, mSPs are formed after 30 min of the self-assembly process (**Figure 1e**). The diameter of these mSPs is 72.4 ± 27.3 nm (**Figure 1k and p**), and they are positively charged with electrokinetic zeta-potential, $\zeta = +25 \pm 7.2$ mV (**Figure S2**, 30 min, dashed box). Their UV-vis spectra of mSPs reveal peaks at 225 nm, 270 nm, and 365 nm (**Figure 1q** -blue line) being red-shifted from the peaks observed for constituent NPs (**Figure 1q**-black line). High-resolution transmission electron microscopy (HR-TEM) images of mSP reveal different directional crystal lattices of NPs (**Figure 1l and m**), confirming NP assembly into mSP the expected total number of NPs incorporated into mSP being *ca.* 6200. The color change of the dispersion (**Figure 1q** inset) from black to yellow implies mSP formation with the partial conversion of the surface FeS₂ NPs into iron oxide. Element maps (**Figure 3**) show that iron oxide layer is located on the surface. Even though the larger aggregations formed after 6 hours, since the optimal time is passed, the structure and size of mSPs remain the same. (**Figure S5 360min** and **S1**). The geometries of the intermediates and final nanoassemblies were also independent of the Cys enantiomer or the use of N-acetyl derivative of Cys (**Figure S6**).

2.4 Multicompartment Supraparticles

SEM-TLD images show that mSPs are nearly spherical particles with a closed surface. By other words, they do not display distinct surface porosity (**Figure 2i**), unlike other inorganic and organic particles being studied⁷⁶ and used as drug carriers.⁷⁷⁻⁷⁹ HAADF images reveal, however, that the continuous surface layer is a shell, and the synthesized SPs have a sophisticated internal structure

(Figure 2j-arrow). For further analysis of the internal organization of the mSP, STEM tomography (Figure 2k and l) and SEM-FIB ion milling (Figure 2m and n) were utilized. Both methods show similar compartmentation where *ca.* 5 nm compartments are interconnected (Figure 2l and n). From these 3D images, the overall size of mSP is 78.04 ± 37.2 nm (See SI 1.3), that is consistent with the TEM images (Figure 1p). The volume of mSP and the compartments are measured $1.01 \pm 0.832 * 10^6$ nm³ and $0.15 \pm 0.048 * 10^6$ nm³, respectively. Approximately 17 ± 5 % of mSP's volume is taken by compartments (Table S3), which is conducive for a high degree of cargo protection.

Element maps reveal the atomic scale organization of these compartments (Figure 3a-e). We found that Fe and S are located inside the mSP, while the surface of mSPs is made of 9.86 ± 1.85 nm thick layer rich in Fe and O (Figure 3e) corresponding to Fe₂O₃ NPs. Approximately 43% of NPs are Fe₂O₃ and located on the surface of the mSPs (Figure 3f-i). To further investigate surface composition, we performed X-ray photoelectron spectroscopy (XPS), and Fourier transform infrared spectroscopy (FT-IR) (Figure S9). High-resolution XPS data (Figure S10) suggests that cysteine bind to the mSP surface in two patterns. Besides the expected Fe-S bond via thiol group, there is also an O-Fe-S bond on the Fe₂O₃ surface. The cysteine binding on the NP was confirmed with FT-IR (Figure S9a). Asymmetric COO⁻ and NH₃⁺ stretching can cause a shift in the position in the IR spectra due to dipole moment change as when cysteine binds on the metal surface with high electron density. The S-H peak disappears in IR spectra, which verifies the covalent interaction of sulfur and iron (Figure S9 a). Therefore, *L*-Cys binding to iron from the thiol group is confirmed, and the positive charge in zeta potential can be explained by the NH₃⁺ groups of the surface ligand (Figure 3j and Figure S2, please see SI 1.4 for a detailed explanation of XPS and FTIR data).

FeS₂ has an indirect bandgap of 0.95 eV,^{80,81} and Fe₂O₃ has a direct bandgap of 2.1 eV,⁸² and thus the mSPs have broad absorption bands with overlapping peaks (Figure 1q). Similar to FeSe₂ NPs,⁸³ we observed strong photoluminescence of mSPs with emission peaks between 320 nm - 650 nm (Figure 3k). Emission peaks at 350-550 nm associated with surface sites^{84,85} (Figure 3l-solid lined box) show

excitation-independent emission spectra and large a Stokes shift of ~50nm. Strong fluorescence of mSP enables the acquisition of confocal microscopy images (**Figure 3 k and l** and see **SI 1.5**) for their tracking and localization in cell cultures.

2.5 Assembly Mechanism

We learned in the previous studies^{55,58,65,86–88} that the control of the self-assembly of NPs into terminal SPs is about control of the balance between several forces with non-additivity relations between them.⁸⁹ The attractive interactions are short-range and include van der Waals, dipolar interactions, hydrogen bonds, coordination bonds. The repulsive interactions are primarily long-range electrostatic forces with some contribution of excluded volume interactions. As shown in **Figure 2c and d**, cysteine layer on NPs increases the attractive forces between NPs and their anisotropy.⁹⁰ We believe that the nanocup formation is associated with the platelet geometry of the constituent NPs and asymmetry of their charge distribution. The electrostatic repulsion between the surfaces of the platelets guides their assembly in a side-to-side fashion instead of forming vertical stacks. Concomitant oxidation of iron on the NP FeS_2 to Fe_2O_3 that may occur on small particles in asymmetrically on top and bottom surfaces, may further increase the anisotropy on the NP and result in the assembly that forms concave structures (**Figure S21**) instead of mesoscale sheets with nanoscale thickness observed under different conditions with reduced rate of oxidation⁷¹ or with NPs of different shape.⁹¹ The oxidation of constituent NPs increases the electrostatic repulsion further (**SI 1.6, Table S4**). The multiple nanocups come together during the reaction and form mSPs resulting in multiple internal cavities in mSPs (**Figure 1c and d**). Size distribution and anisotropy on these nanocups result in the distribution of sizes in the compartment, but the overall dimensions and the total number of NPs in mSPs remain self-limited.

2.6 Graph Theoretical Description

The structure of mSPs and other nanoassemblies possible in this system can be described by methods of graph theory (GT)⁹² whose an implementation to nanoscale structures is similar to GT indexes

used for organic molecules.⁹³ The GT-based structural models provide a method to describe different nanostructured assemblies taking into account both the geometry of the constituent NPs and their resulting assembly patterns (SI 1.7). The benefit of the GT structural models is that they are uniformly applicable to all types of nanoassemblies – organic, inorganic, and biological – which can be used for their comparative evaluation and structural design.

The GT representations of NPs, nanocups and mSPs are given in (Figure 4a-c). The minimal GT representation of disc-like NPs is K_3 graph (Figure 4a and S13a). The GT representation of nanocups in Figure 4b reflects the fact they are formed by edge-to-edge merger of nanoplatelets. Mesoscale nanosheets with continuous inorganic phase are represented by the same K_3 graph as the nanoplatelets. However, they also have a concave shape overall. Unlike ‘flat’ nanoscale sheets (represented by K_3) and similarly to inorganic ribbons with a twist (represented by K_5), the non-random 3D shape of the nanocups is reflected by the two additional nodes. GT representations of mSPs describes the fact that they carry a shell comprised of iron oxide NPs (Figure 4c). Compartments in mSPs are graphically represented graph loops (closed circle with a node). The self-assembled mesoscale nanosheets (K_3) assembled from NPs are assumed to be randomly distributed within the SP filling the remainder of the space (Figure S19d). Similarly, to self-assembled particles of Au-S nanoplates with *L*-cys surface ligands,⁹² we calculated the complexity index (*CI*) for each structure (see SI 1.7 for detailed calculation) to operate with quantitative rather than notional concept of complexity.

mSPs display obvious structural similarities and comparable complexity with human adenovirus (Figure 4d). This point can also be strengthened by the fact that typical viral structural capsid proteins have a mean diameter of 5 nm and a mean thickness of 2 nm,⁹⁴ which is similar to constituent NP size and thickness here, with self-assembly in stable spherical shell.⁹⁵ Furthermore, adenovirus and mSP has similar loading capacity where adenovirus can be loaded up to 8kb⁹⁶ and mSP can be loaded >6kb (SI1.13, Table S5).

2.7 DNA Encapsulation

The process of mSP formation facilitates the use of compartments for cargo packing and delivery. To demonstrate cargo loading of the compartments within mSPs, we added pEEB Cherry plasmid DNA (pDNA) at the stage of nanocup self-assembly. Allowing subsequent maturation of nanocup into mSPs, the final particles containing DNA cargo, abbreviated here as mSP-pDNA, were analyzed for DNA presence and localization. UV-Vis and circular dichroism data do not show significant differences in the spectra between mSPs and mSP-pDNA (**Figure 5a-b**) since the absorption of mSP and nucleic acid overlap. In addition, there is the possibility that structural change of the nucleic acid in mSPs may alter its hyperchromicity, similar to viruses.^{97,98} Dynamic light scattering (DLS) data of mSP-pDNA also shows that the zeta potential of loaded and empty mSPs are the same (**Figure 5c**) indicating that DNA is not located on the mSP surface. STEM, TEM, and HAADF STEM images (**Figure S15**) show minimal differences in size/shape of mSP size with and without DNA. Some alterations in organization of the internal compartments in presence of pDNA are possible but will require extensive studies with 3D reconstructions of the multiple mSPs. No DNA in the supernatant after formation and separation of mSP-pDNA was also found (**Figure 5a**). All these data suggest complete pDNA encapsulation, which was confirmed via electrophoresis mobility shift assay (EMSA), where naked DNA moves freely in the gel, but its mobility is restricted if it is bound to another entity. EMSA proves the DNA present in the system by first showing bands for pDNA only but not the mSPs only lanes in the gel; second, stained DNA remains in the well (restricted mobility into the gel) of the mSP-pDNA lane due to encapsulation by heavy mSP (**Figure 5d**). Note that mSPs are positively charged, and they move in the opposite direction; however, when they are loaded with pDNA, DNA and mSP want to move in different directions, and that causes them to be stuck in the well. The addition of DNase prior to gel electrophoresis indicates that DNA is protected from digestion within the mSPs (**Figure 5d**). The absence of a free pDNA band in the mSP-pDNA line, along with no DNA in the supernatant of the reaction, may also suggest that mSPs show approximately 100% encapsulation and protection of pDNA. The final evidence for DNA

encapsulation within the mSP is elemental mapping where phosphate signal specific to DNA stays inside the iron oxide layer of mSP (**Figure 5e**). These multiple lines of evidence confirm that DNA is successfully encapsulated in the mSP. The driving force of the encapsulation of pDNA is electrostatic interaction between the negatively charged pDNA and positively charged constituent NP that allows the multicompart ment supraparticles (mSPs) to trap pDNA during their maturation. The average number of pDNA per mSP is calculated ~80.

DNA release assay was also performed with UV spectroscopy to determine what conditions and how long it takes to release the DNA from the mSP-pDNA complex. pDNA release assay of mSP-pDNA was conducted at two different pH (~5.5 and 7.4) in two different media -water and phosphate buffer. On the other hand, pH 5.5 is used to model the endosome environment. The relative pDNA release was quantified at 260 nm (**Figure 5f-g**). Encapsulated pDNA is released at acidic conditions (pH 5.5 in water and pH 5.8 in PBS) within 2 hours (**Figure 5g**) as mSP starts to degrade (**SI 1.9**). Importantly mSP-pDNA remains stable even after 50h in water and PBS at pH 7.4 (**Figure 5f** black and red lines) at 37 °C. Electrophoresis was employed for intact pDNA release (**Figure 5h**).

2.8 Cytotoxicity, Cellular Uptake, and Transfection

For cellular experiments, the number of particles per cell must be controlled. We want to provide as many particles as possible to maximize transfection while avoiding cytotoxicity. Even though toxicity is not expected with these mSPs, the cytotoxicity may still originate from the nature of NPs. So, we tested how mSP-pDNA affects the viability of human cells (HEK293T) for different exposure times, concentrations, and cell numbers (**Figure 6a, b**). The toxicity of mSP-pDNA on cells compared to the control group is insignificant if the particle: cell ratio is kept at 4000 or low for 24h (**Figure 6a** dashed lines show the thresholds where $p\text{-value}>0.05$). It is noticeable that 1000x concentration decreases cell viability significantly since the particle: cell ratio is 4×10^4 or higher. After 48h of incubation in the

presence of 10x mSP-pDNA, cell viability decreased by *ca.* 22% if the particle: cell ratio is higher than 2000 (**Figure 6b**, dashed lines show the threshold). For transfection experiments, HEK293T cells were treated with mSP-pDNA with 1000 particle: cell ratio for specific time intervals from 6h to 24h.

Based on the cytotoxicity assay, we calculated the particle concentration of mSPs, that is ~1000 mSPs per cell, giving a sufficient number of particles without creating cytotoxicity (**SI 1.10**). For cellular uptake analysis, we used the advantage of mSP fluorescence and calculated the mean fluorescent intensity of mSPs under confocal images. mSPs gave the highest emission intensity when they excited at 475 nm and 500 nm in the window of 520-700nm emission wavelengths (**Figure 3k- and l and SI 1.5**). Thus, confocal images of mSP-treated cells are observed at 475 nm (**Figure 6c**) and 500 nm (**Figure 5d**). We are using two different excitation wavelengths to confirm that the signal is coming from mSPs and that it is not an artifact of the other cell compound. With increasing incubation time, the mean fluorescence intensity per area of an image increased gradually, reflecting cellular uptake (**Figure 6e**). For the first 2 hours, the cellular uptake was faster than in the following time periods. In 6 h, the cellular uptake gradually reached saturation, where is the percentage of fluorescence-positive cells no longer increased. mSPs attach to cells in 1h; even after 3x washing, we can see particle attachment on the cell surface (**Figure S18**). The fluorescence intensity of particles in cells does not change much between 4h-12h (**Figure S19 a-b**); untreated cells show no fluorescence at the same laser intensity (**Figure S19c**).

Transfection is also expressed as the mean fluorescent intensity of confocal images of reporter protein (pEBB cherry-red color). Even though cellular uptake reaches saturation at 6 h, releasing and transcription of pDNA takes time. Therefore, we started to see red-emitting cells after 9 hours (**Figure 6h**). Confocal images of mSP-pDNA transfection can be seen in **Figure 6j-l**. The comparison between mSP and lipofectamine is not statistically different (**Figure 6i, Figure S20**). However, mSPs can condense DNA, protect it against degradation, enter the cell and release it in the cytosol (**Figure**

5f-h). A fine balance between extracellular protection, intracellular release, and biodegradation is crucial. The presence of iron in mSPs may facilitate cellular uptake due to van der Waals interactions of the mSPs and cellular membrane. This feature may decrease the excessive membrane potential change that occurs with liposomes. The release of cargo after transmembrane transport is facilitated by the spontaneous disassembly of mSPs in the cells. Attractive-repulsive forces between constituent NPs control mSP stability. Disassembly occurs because of the shift in the balance between attractive and repulsive forces that keeps NPs together when they self-assemble outside the cells. Once mSPs entered the cell, a drastic change in pH and dielectric constant (ϵ) occurs.⁹⁹ For example, the dielectric constant for cytosol of human red blood cells is reported to be <50 ,¹⁰⁰ while for water and interstitial fluid, $\epsilon = 78$. The reduced dielectric constant is associated with an *increase* in electrostatic forces in accord with the Coulomb law. Therefore, the increase of inter-NP repulsion¹⁰¹ leads to mSP disassembly. Concurrently, pH differences from outside (7.4) to inside (5.5) of the cell cause disassembly and DNA release in **Figure 5f-h**. The increased osmotic pressure can lead to the ‘burst’ of the mSPs in the cytosol.

2.9 Thermal Stability of Biological Cargo

We wanted to check if mSP can stay stable under extreme conditions for a long time. We kept mSPs at $-20\text{ }^{\circ}\text{C}$ and room temperature (RT) for more than 4 years and at $70\text{ }^{\circ}\text{C}$ for 50 hours. After bringing them to RT, we checked for their stability via UV-Vis spectra (**Figure 7a**), DLS (**Figure 7b**), and TEM (**Figure 7c**). UV-Vis spectra and zeta potential data did not show any significant changes between mSPs kept at different temperature (**Figure 7a**). Only difference we observed is mSP at $70\text{ }^{\circ}\text{C}$ has a little larger size (**Figure 7b-size**), this can be due to completion of unmaturing particles or aggregation of smaller particles as can be seen TEM images (**Figure 7c**). Since we did not see any changes for mSP, we tested SP-DNA for its ability to protect DNA at high temperature ($70\text{ }^{\circ}\text{C}$) for 50 hours and transfect the cells (**Figure 7d-e**). These images show that DNA is protected at $70\text{ }^{\circ}\text{C}$ by mSPs with giving the red color of the reporter protein (pEBB cherry).

3. Conclusion

FeS₂ NPs self-assemble into compartmentalized mesoscale particles with multiple internal cavities via reorganization of these cup-shaped metastable nanoassemblies. The complexity and organization of mSPs are similar or identical to those observed in viruses, which led us to conclude that the nanoscale compartments can effectively protect the cargo against heat and other environmental factors representing one of the biggest bottlenecks for deployment of vaccines.¹⁰² We demonstrated that mSPs can protect and deliver the DNA cargo against temperatures as high as 70 °C. We expect that application of mSP can considerably improve the accessibility to vaccine.

Based on the simplicity of the mSP assembly-disassembly mechanism, we expect the possibility of using mSPs for gene therapies and other area of medicine as well as biotechnology. However, the stability of the molecule must be considered. For example, mRNA encapsulation, similar to the current SARS-CoV-2 vaccines,^{103,104} may require additional modifications¹⁰⁵ such as 5' cap¹⁰⁶, pseudouridine modifications¹⁰⁷ or sequence-optimization¹⁰⁸ to increase the stability before encapsulation. In addition, the electrostatic interaction of NPs and mRNA has to be balanced to allow complete release in the cell.

4. Experimental Section/Methods

Materials: All materials except plasmid were purchased from commercial sources: Iron III Chloride (FeCl₃), sodium sulfide nonahydrate (NaS₂·9H₂O) and L/D-cysteine and N-Acetyl cysteine were purchased from Sigma-Aldrich (St. Louis, MO, USA); absolute ethanol from Fisher-Scientific (Hampton, NH, USA); grids with ultra-thin carbon film on holey carbon film support for transmission electron microscope (TEM) and carbon film only for scanning transmission electron microscope (STEM) analysis purchased from Ted Pella (Redding, CA, USA); disposable folded capillary cells for dynamic light scattering measurements were purchased from Malvern Instrument (Worcestershire, UK). Hellma fluorescence cuvettes were purchased from Sigma Aldrich for UV-Vis, Fluorescence, and CD measurements. All cell culture materials were purchased from Gibco-BRL Inc. (Gaithersburg,

MD, USA) unless otherwise stated differently. The pEBB-Mchery plasmid is used to transform *Escherichia coli* and amplified plasmid extracted with plasmid isolation kit (Invitrogen™ PureLink™ HiPure Plasmid Filter Maxiprep Kit).

Synthesis of NPs: 0.5×10^{-3} M L-cysteine and 10^{-2} M iron III chloride in 100 ml DI water under magnetic stirring on ice under air. 10 ml of 5×10^{-1} M sodium sulfate nano-hydrate was then dropwise added to the solution under constant magnetic stirring. Once color changed to black, reaction stopped, and NPs were collected by centrifugation at 14K for 1h, washed three times with absolute ethanol. We dried the particles entirely at room temperature to make sure no trace of ethanol. Particles then dissolved in Milli Q water for further experiments.

Compartmentalized synthesis of mSPs: mSPs obtained by increasing the NP reaction temperature to room temperature. After 30 min, the color changed from black to yellow and the reaction is stopped. mSPs are collected by centrifugation 10k for 15min, and subsequently washed three times with absolute ethanol. For the time-dependent experiment, the reaction stopped at specific time points. We dried the particles entirely at room temperature to make sure no trace of ethanol. Particles then dissolved in Milli Q water for further analysis and experiments.

Cup-like intermediate structure synthesis: The time-dependent experiment showed that intermediate structures form between time 0 (right after the sulfur source added to reaction) and 15min when the reaction is at room temperature. For collecting cup-like intermediates, the reaction stopped at 15min and washed three times similar to mSPs.

Encapsulation of pDNA into mSPs: The system was slowed down by stopping the mSP reaction at 15 min to utilize the compartments of the mSPs. At this point, 150 μ g plasmid (pEEB cherry – 6073bp) is added dropwise to the system, and the reaction was allowed to complete the mSP formation under magnetic stirring. After 15 min (total of 30min), mSPs containing DNA (mSP-pDNA) were collected and washed as usual.

Calculating amount of DNA molecule in mSP: This calculation is based on the assumption that the average weight of a base pair (bp) is 650 Daltons.

number of DNA copies = (amount in g* 6.022×10^{23}) / (length* 650)

150 μ g pDNA = 2.29×10^{13} pDNA molecule per system

Since the system has $\sim 3 \times 10^{11}$ particles per system, it is calculated that there are ~ 80 pDNA molecules per mSP.

Particle Characterization: UV-Vis measurements are acquired by an 8453 UV-Vis Chem station spectrophotometer produced by Agilent Technologies. Zeta potential of mSPs was measured at 25°C using a Zetasizer Nano ZS instrument (Malvern Instruments Ltd, Malvern, Worcestershire, UK). Circular Dichroism (CD) spectra were obtained by a JASCO J-815. TEM images obtained by utilizing JEOL 3011 high-resolution electron microscope equipped with a CCD camera and a field emission gun (FEG) operating at 300 kV. SEM images were obtained with FEI Helios 650 Nanolab SEM/FIB. STEM images obtained with JEOL 2100 Probe-Corrected Analytical electron microscope equipped with a Gatan Ultrascan 1000 CCD TV camera and a field emission gun (FEG) operating at 200KV. The Fourier transform infrared spectroscopy (FTIR, Thermo-Nicolet IS-50); energy dispersive X-ray spectrometry (EDS, FEI Helios 650 Nanolab SEM/FIB and JEOL 2100F) and X-ray photoelectron spectrometry (XPS, Kratos Analytical AXIS Ultra) and X-Ray diffractometer (XRD, Rigaku Rotating Anode with Cu K α radiation generated at 40 kV and 100 mA) were used to exam the composition of particles. Fluorescence data is obtained by a Jobin Yvon Horiba FluoroMax-3 instrument.

Particle size: Particle size is calculated with image J analysis with number of TEM images. The total number of particle (n) is measured for calculatios. n for mSP is 1276, n for cup-like structures is 300 and n for NP is 150. Nanoparticle Tracking Analysis (NTA) was also conducted for confirming size of mSP in aqueous environment. NTA data were obtained by Malvern NanoSight NS300 on aqueous dispersions.

Phase Identification: Multiple diffraction rings of mSPs are obtained, and d-spacing of each diffraction rings calculated with image-J. All results are recorded and sorted with decreasing d-spacing, here $\pm 0.1 \text{ \AA}$ is considered as a measurement error. The list of d-spacing of mSPs is compared with known samples containing iron, sulfur, and any combination of these three elements.

Excitation-Emission Matrix: Excitation-emission matrix (EEM) is a 3D landscape with a z-axis measuring the intensity where red color shows the highest intensity, and purple color displays the lowest intensity. If the material is fluorescent, emission peaks of different excitation wavelengths should be stable in the scanning. Likewise, we excited mSP suspension from 200 nm to 600 nm with 10 nm increments.

Electron Tomography: The electron tomography studies at room temperature were carried out on two different systems:

- 1) JEOL 2100 Probe-Corrected Analytical electron microscope equipped with a Gatan Ultrascan 1000 CCD TV camera and a field emission gun (FEG) operating at 200KV and
- 2) FEI Helios 650 Nanolab SEM/FIB with slice and view software.

For JEOL 2100, a series of 2D projection images were recorded by tilting the specimen from -65° to 70° for increments of 1° . A tomography reconstruction software package Etomo was used to align the tilt series. The surface and volume rendering were generated using the Avizo software.

For SEM tomography, slice, and view software employed. The particle cluster on a silicon wafer was coated with first carbon and then platinum to protect the particles from ion beam damage. The area is milled with an ion beam every 3 nm, and images were taken. The images taken with FEI Helios 650 Nanolab SEM/FIB were aligned, and the surface and volume rendering were generated using the Avizo software.

Surface area and volume calculation: 17 polydisperse mSPs were grouped based on location in the cluster and color-coded. Number of mSP, each mSP size in diameter, average volume, and surface area of each color-coded area were calculated within Avizo software.

Calculation of the number of compartments in an mSP

We considered the shape of the individual compartments and whole compartment unit structure are sphere to simplify the calculations. We calculated the number of compartments in mSP in a way that a volume of a sphere is highly packed with smaller spheres. Based on TEM analysis V_{SP} can be calculated ($R_{SP} = 36.2\text{nm}$, $V_{SP} = 1.98 \times 10^5 \text{ nm}^3$). Therefore, we can calculate the volume of compartments (V_{SC}) as $3.37 \times 10^4 \text{ nm}^3$ (17% of the V_{SP}).

$$V_{SC} = 0.17 * 1.98 * 10^5 \approx 3.37 * 10^4$$

Kepler conjecture the highest packing density of same-sized spheres in the three-dimensional space is $\frac{\pi}{3\sqrt{2}} \approx 74.048\%$. We also know the sphere volume is $\frac{4}{3}\pi r^3$.

Using the diameter of compartments ($r_{IC} = 2.6\text{nm}$ - tomography analysis ($d_{IC} = 5.2\text{nm}$)) number of compartments per mSP can be calculated to be ~ 340

$$V_{SC} * 0.74048 / V_{IC} \approx 340$$

In where V_{SC} : Volume of whole compartments in mSP, V_{IC} : Volume of individual compartments, and V_{SC} is $3.37 * 10^4 \text{ nm}^3$, and V_{IC} is $0.74 * 10^2 \text{ nm}^3$ (**Figure S8**)

The number of NPs in an mSP: Since mSPs are self-assembled with multiple compartments, we conclude that NPs should form chains. Therefore, we calculate the number of NP in a mSP in a way that the plane is highly packed with circles. The densest packing of circles in the plane is the Steinhaus's hexagonal lattice packing is $\frac{\sqrt{3}\pi}{6} \approx 90.689\%$. We consider the packing density of NP in an

mSP is $\approx 90\%$ and we know the volume of a cylinder is $\pi r^2 h$, where $d=4.5\text{nm}$ and $h=1.5\text{nm}$.

Therefore, number of NPs per mSP can be calculated to be $\sim 6,200$.

$$V_{\text{NP}} = \pi \cdot 2.25^2 \cdot 1.5 = 23.85 \text{ nm}^3 = 0.024 \cdot 10^3 \text{ nm}^3$$

$$0.9 \cdot (V_{\text{mSP}} - V_{\text{SC}}) / V_{\text{NP}} = \sim 6,185$$

$$\text{Where } V_{\text{mSP}} - V_{\text{SC}} = 1.65 \cdot 10^5 \text{ nm}^3$$

$$1.65 \cdot 10^5 \text{ nm}^3 \cdot 0.9 = 1.48 \cdot 10^5 \text{ nm}^3$$

The top two layers ($\sim 8.9\text{nm}$) of mSPs are Fe_2O_3 NPs, therefore approximately 43% of NPs are Fe_2O_3 NPs.

Lambda scanning in confocal microscopy: Super-resolution Leica SP8 MP Confocal STED microscope is utilized for lambda scanning. A lambda scan is an acquisition of an emission spectrum using spectral detectors, and it records a series of individual images of the sample within a defined wavelength range. Lambda scan is performed between 470-570 nm excitation range with a white light laser to find the best excitation wavelength. The size of the emission window is kept 50 nm long, and it is shifted 20 nm further along with excitation wavelength for the sake of the detector. The intensity of each image is quantified and graphed with Las X software. As the white light laser range is 470-670 nm, we performed the lambda scanning starting from 470 nm and ending at 570 nm (no emission after 570nm).

Cell Culture: HEK293T cells were purchased from American Type Culture Collection ATCC (#CRL-11268). Cells were maintained at 37°C with 5% CO_2 in Dulbecco's Modified Eagle's Medium (DMEM) media supplemented with 10% fetal bovine serum and 1% penicillin/streptomycin (Thermo Fisher Scientific, Waltham, MA) and passaged every 3-4 days at 80% confluency. Cell cultures are tested regularly, and no mycoplasma infection was found.

Cell Viability Assay: 100µl HEK 293T cells were seeded on cell culture treated 96 well-plate (in the concentration of from 100.000 cells/ml serial dilution to 82 cells/ml and incubated at 37C° for 24 hours Then, medium discarded and cells were washed with PBS 2 times to remove non-attached cells. 90µl fresh media added along with 10µl mSPs in the concentration of 10x and 1000x and incubated for 24h or 48h. Promega™ CellTiter 96™ Nonradioactive Cell Proliferation Assay (MTT) was conducted as described in the protocol. Shortly, 15µl dye solution added to cells and incubated for 4 h, then 100µl stop/solubilization solution is added, and then sealed and incubated at 37C° overnight to allow complete formazan product solubilization. Tetrazolium salt in the dye solution converted into the formazan by living cells, and the solubilization solution solubilizes the formazan product. The next day, plate reader (BioTek Synergy 2 Plate Reader, BioTek Instruments, Inc., Winooski, Vermont, USA) utilized to record absorbance at 570nm. As a blank absorbance of mSP solutions in media used and subtracted from all samples. All experiments were repeated three times. The results were expressed as mean ± SD (n = 5).

Cellular Uptake and Transfection: The Hek293T cells were seeded in a Lab-Tek® chambered cover glass system at 4.8×10^4 cells per well (8 wells per chamber) and cultured for 24 h to achieve 70% confluence. The media is discarded, and cells washed two times to remove unattached cells. 20 µL of mSP and mSP-pDNA dissolved in media were added for cellular uptake and transfection, respectively. Wells are completed to 200 µL with media. Treated cells were incubated for 30min up to 48h. The cells were washed two times with PBS and fixed by 4% paraformaldehyde for 1h, and fixative was aspirated, and the cells washed with PBS three times. Nuclei were labeled by Prolong® Gold Antifade Reagent with DAPI and store in the dark until imaging. Cells were imaged using Leica SP8 MP Confocal STED microscope for cellular uptake of SPs. Different confocal images were taken from different locations of a plate in a matrix of 3 by 5 at 475 and 500 nm excitation wavelength for cellular uptake experiment. Mean fluorescence intensity quantified by using FIJI software. Instead of threshold apply, we subtracted an empty area of an image of cells without particles taken by exact

same configurations. The data were normalized, and results were graphed based on each time point in origin. This imaging was repeated on three independent experiment sets for each time slot.

For transfection, we used same cell density with aiming 1000 SP-DNA per cell ratio. For comparison we used Lipofectamine 3000® that was obtained from Life Technologies (Invitrogen, Carlsbad, USA). The product protocol followed exactly as described. Three independent transfections were repeated for both SP-DNA and Lipofectamine. Nikon A1 with Texas red filter was utilized for live cell imaging after 6-24h. Fluorescence intensity from these images were quantified via Image J. All errors given represent standard deviations.

Mobility Shift Assay: 1% agarose gel was prepared with gel red, and 10 μ L samples (mSP, mSP-pDNA, pDNA) mixed with 10x loading dye (Thermo Scientific™ 6X TriTrack DNA Loading Dye). Samples were then loaded to wells along with 2 μ L 1K ladder (Thermo Scientific™ GeneRuler 1 kb DNA Ladder). Gel run in gel apparatus (Bio-Rad) at 35V for 2h. Gel imaged with a gel imaging instrument (Bio-Rad).

DNA release Assay: mSP-pDNA incubated in two different pH (5.5 and 7.4) in two different solvents (water and Phosphate Buffer) for 0-48h every 20 min for the first 2 hours and for 6, 12, 24 and 48h, each time intervals and absorbances were taken with UV spectroscopy (NanoDrop 2000, Thermo Scientific). mSP in water or PBS used as a reference, and relative absorbances recorded for percentage calculation. pH adjusted with HCl and NaOH.

Statistical Analysis: The data were summarized as means \pm standard deviation based on experimental values obtained in multiple measurements. Where necessary, the statistical variations (p values) between the group means were evaluated by one-way ANOVA in R.

Supporting Information

Supporting Information is available from the Wiley Online Library.

SI 1.1-1.14

Figure S1-S21

Table S1-S5

Video S1-S4

Acknowledgment

The authors would like to thank the University of Michigan's the Michigan Center for Materials Characterization and Microscopy & Image Analysis Laboratory Cores for the use of instruments and staff assistance. The authors also thank Prof. Colin Duckett for the first batch of pEBB-mcherry plasmid. Funding Sources: The support from the Taubman Institute to JSV NIH grant # K08 AI128006, and support from Turkey Ministry of National Education to ESTE & AE are gratefully acknowledged. Additional financial support acknowledged to the University of Michigan College of Engineering, NSF grant # DMR-0723032, #DMR-0420785. Schemes are created with BioRender.com

Author contribution

ESTE designed and conducted experiments. AEE assisted mSP synthesis and contributed to cell experiments. DAV calculated the GT models. UK and JSV were involved in discussions on cellular and bacterial work. ESTE and NAK wrote the paper. NAK conceptualized the research.

Corresponding Author

Address correspondence to **J. Scott VanEpps**, University of Michigan Medical School, Department of Emergency Medicine, North Campus Research Complex, Building 14, Room 117, 2800 Plymouth Road, Ann Arbor, MI 48109, phone (734) 763-2702 Email: jvane@med.umich.edu; and **Nicholas A. Kotov**, University of Michigan, Department of Chemical Engineering, NCRC Building 10, Room A159, 2800 Plymouth Rd, Ann Arbor, MI 48109, phone (734) 763-8768. Email: kotov@umich.edu.

Abbreviations

SP, Supraparticle; mSP, multicompartiment supraparticles, pDNA, Plasmid Deoxyribonucleic Acid; NP, Nanoparticle; ER, Endoplasmic Reticulum; TEM, Transmission Electron Microscopy; HR-TEM, High-Resolution Transmission Electron Microscopy; NTA, Nanoparticle tracking analysis; HAADF, High Angle Annular Dark Field; STEM, Scanning Transmission Electron Microscopy; SAED, selected area electron diffraction; XRD, X-Ray diffraction; SPN, supernatant; NAC, N-Acetyl cysteine; EEM, Excitation-Emission Matrix; DMEM, Dulbecco's Modified Eagle's Medium; HEK, Human Embryonic Kidney; PBS, phosphate-buffered Saline, TLD, Through the Lens Detector

Author Manuscript

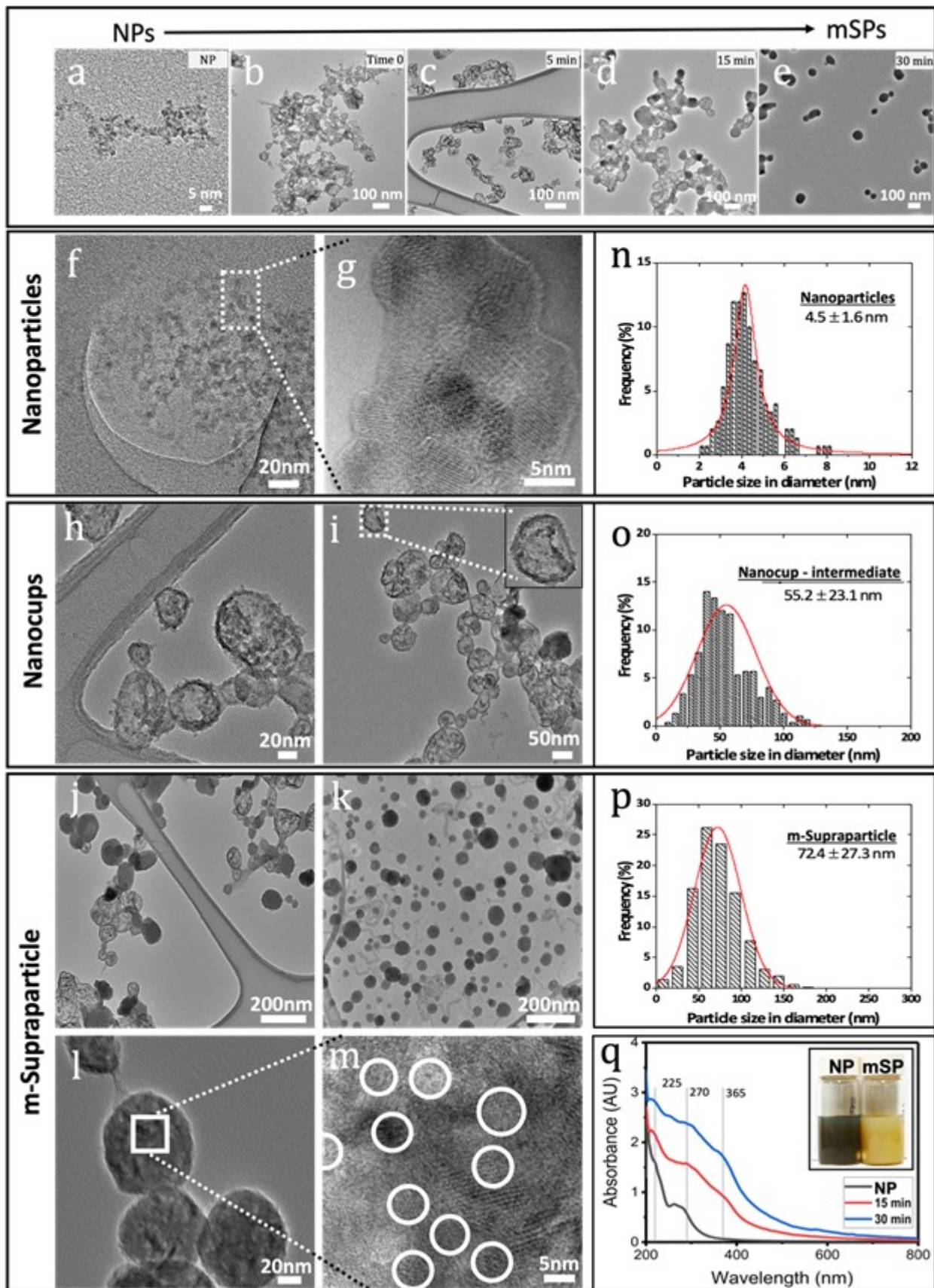


Figure 1: TEM study of mSPs and their self-assembly process. (a-m) TEM images and (n-p) size distribution analysis of the self-assembled structures. (a-e) Intermediate nanoassemblies on the pathway from NPs to mSPs in 30min. (f-g) TEM images of constituent NPs. (h-i) Nanocup intermediates at 0-15 min without mSPs; and (j) with partially formed mSPs at 15 min. (j-l) Mature mSPs (30 min). (m) Constituent NPs in the mSP. (n) NPs are 4.5 ± 1.6 nm in diameter, (o) Nanocup intermediates are 55.2 ± 23.1 nm in diameter, and (p) Mature mSPs are 72.4 ± 27.3 nm in diameter. (q) UV-Vis spectrum of NPs, nanocups (15 min), and mSP (30 min); insert - photograph of NP and mSP (after 30 min of assembly) dispersions in water.

Author Manuscript

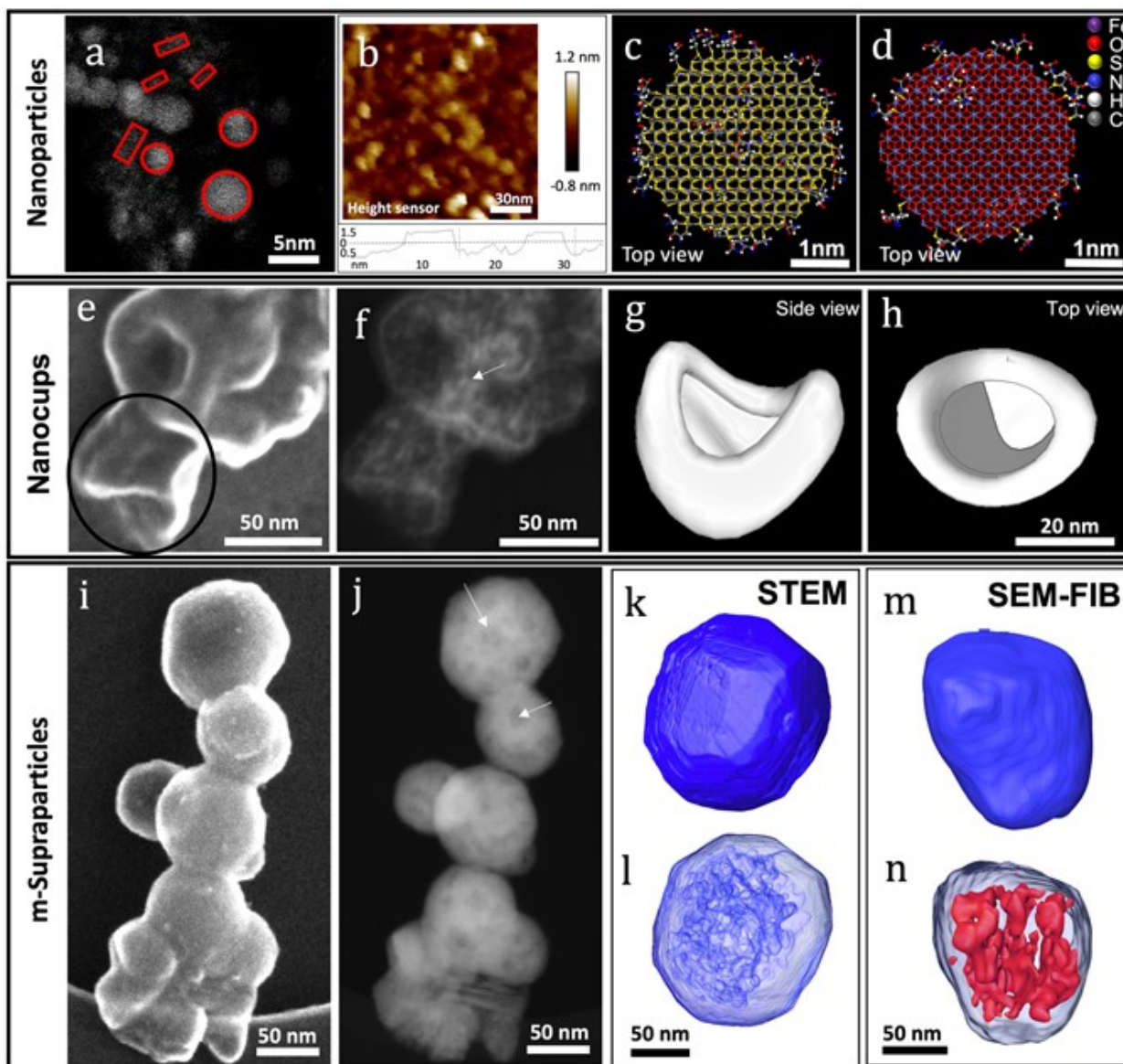


Figure 2: Three-dimensional structure and compartments of (a-d) NPs, (e-h) nanocups, and (i-n) mSPs. (a) Darkfield STEM image of NPs that are seen from various angles. (b) AFM data of NPs. This data suggests disk-like geometry and height of NPs consistent with AFM data. (c-d) Atomic structures of (c) iron sulfide NP and (d) iron oxide NP with *L*-Cys surface ligands bound to iron via the thiol groups. (e-f) SEM images of nanocup intermediates acquired with (e) a TLD and (f) HAADF detectors, respectively. Constituent NPs in the nanocup intermediate are marked with an arrow in (f). (g-h) Three-dimensional model of nanocup that is highlighted with a black circle in (e). (i-j) SEM images of mSPs acquired with (i) TLD detector and (j) HAADF detector. Compartments of mSPs in HAADF images marked with arrows. (k-n) Reconstructed tomography images of mSPs, (k-l) acquired by STEM tomography, and (m-n) acquired by SEM-FIB slice and view. (l and n) reveal continuous compartments in the mSPs, red-colored in (n).

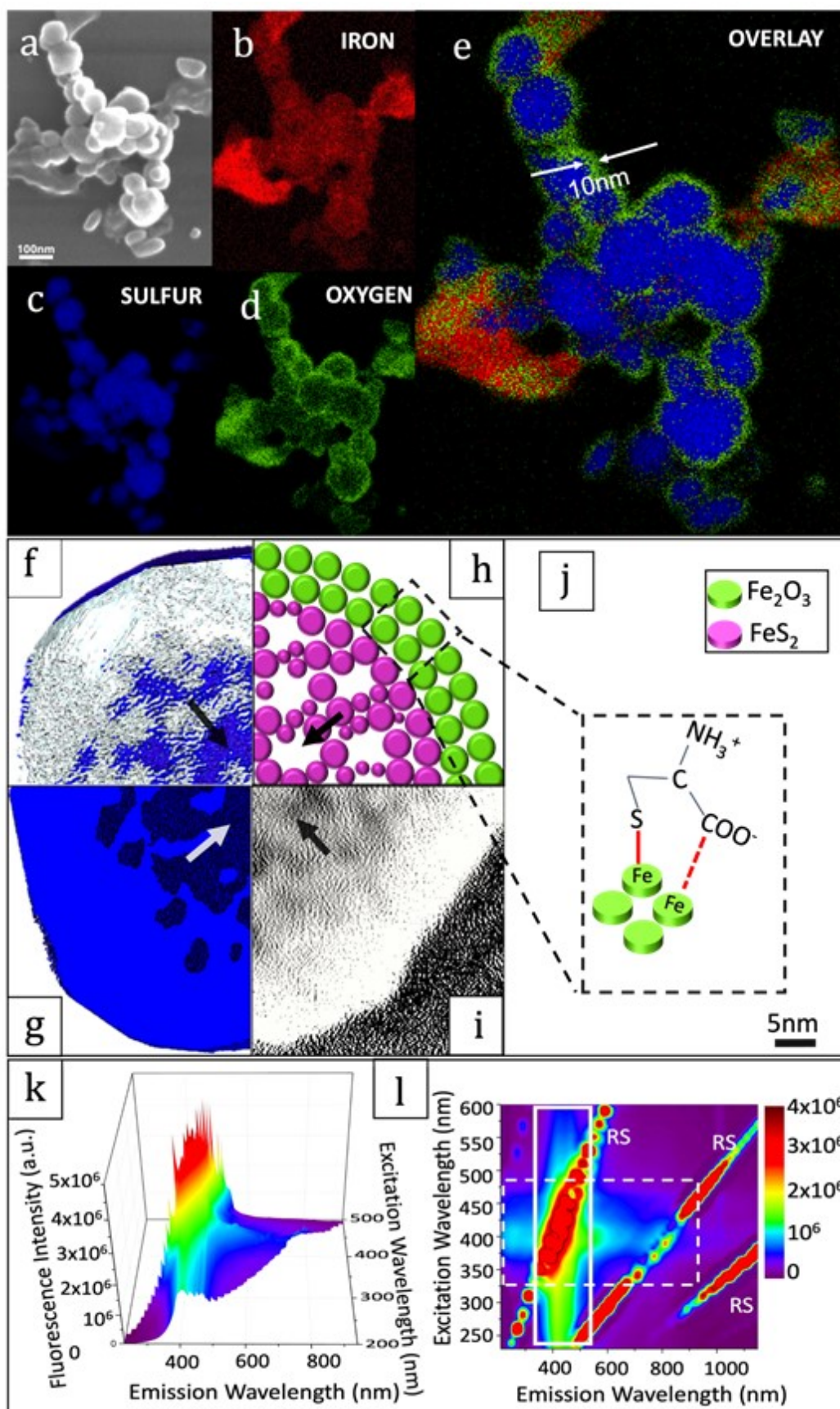


Figure 3: Elemental analysis and cross-section of mSPs. (a) An SEM image of mSPs (b-d) Elemental analysis of the mSPs and location of iron, sulfur, and oxygen elements in mSPs. (e) overlay image of three elements. This image shows that iron oxide nanoparticles are at the surface and create a shell on the mSPs. mSPs contain continuous internal compartments protected from the outside by Fe₂O₃ NP membrane 9.86 ± 1.85 nm thick. Cross-section of reconstructed mSP (f) surface and (g) volume rendering acquired by STEM tomography. (h) Scheme of cross-section where green disks show two layers of Fe₂O₃, and magenta disks show FeS₂ nanoparticles. (i) orthogonal slice of STEM tomography. Black arrows in each image (f-i) show compartments. (j) Magnified representation of Fe₂O₃ NP with L-cysteine on the surface. (k) 3D representation of fluorescence spectra and (l) contour map Excitation-emission matrix (EEM) spectra of the mSP suspension. RS is Rayleigh scattering peak, $\lambda_{ex} = \lambda_{em}$. The solid lined box in (l) shows stable picks (350-550nm) with broad-range excitations (200-600nm). The dashed box in (l) shows the excitation range gives the highest emission.

Author Manuscript


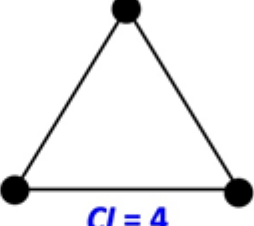

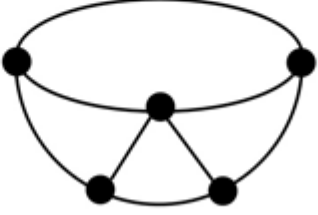

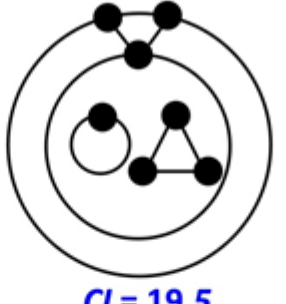


a	Scheme	GT Models	Explanation
Nanoparticles		 <i>CI = 4</i>	Constituent NP is a disc-like nanoparticle; and is represented as a K3 graph, which represent a 2-D structure
Nanocups		 <i>CI = 18.75</i>	Like inorganic ribbons with a twist (represented by K ₅), the non-random 3D shape of the nanocups is reflected by the two additional nodes
mSPs		 <i>CI = 19.5</i>	mSPs are represented as a combination of compartments (See Fig. 19c) and a hollow shell layer comprised of iron oxide disc-like NPs
Adenovirus		 <i>CI = 25.125</i>	Protein shell represented as 3D hollow core (K4 in a loop) with grafted K2 spikes at the vertices.

Figure 4: Minimal GT representations for nanoscale structures: (a) disk-like NPs, (b) nanocups, (c) mSPs, (d) adenovirus along with the complexity indexes (CI) are given in blue font.

ADT

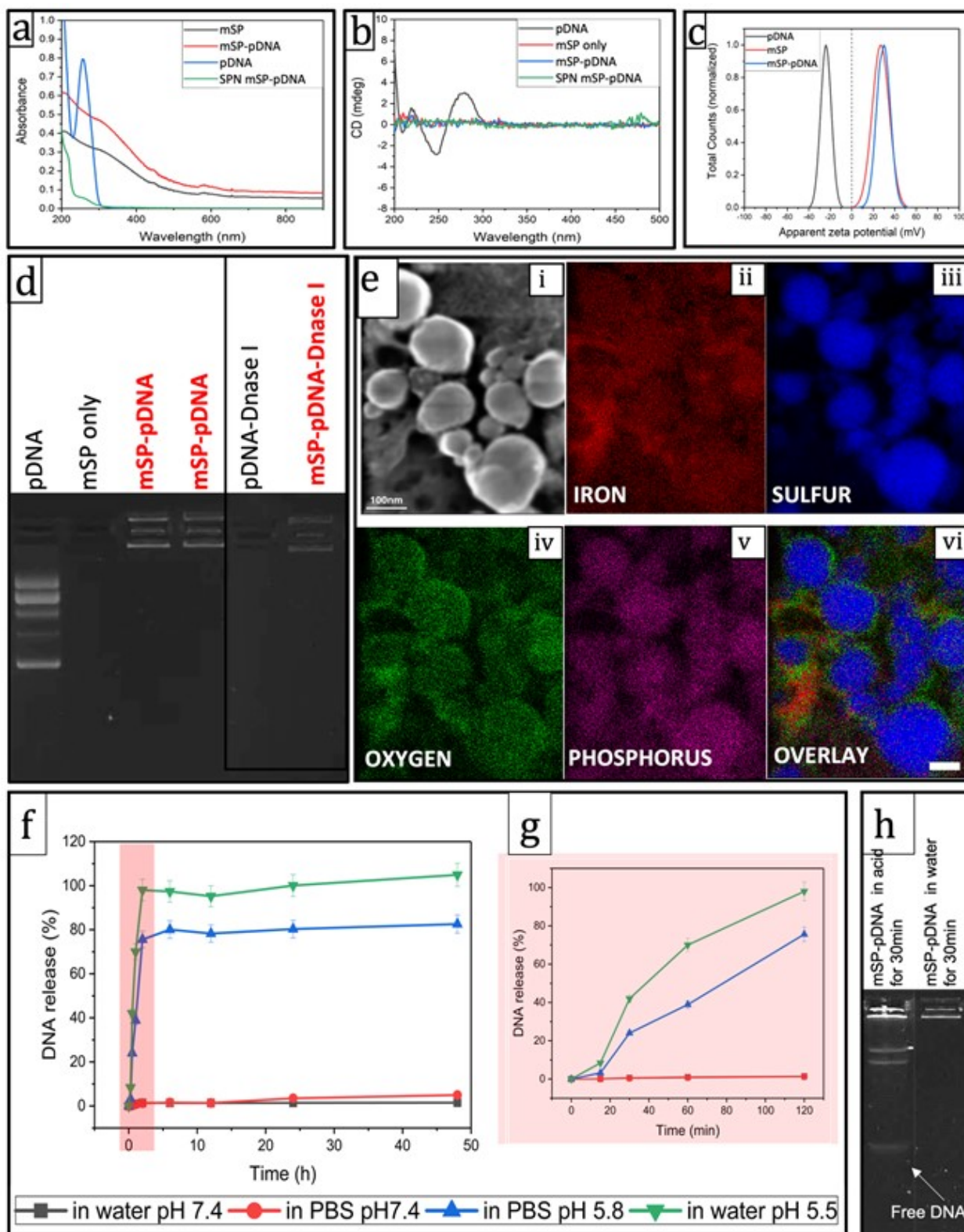


Figure 5: DNA encapsulation and release. (a) UV-Vis spectra (b) Circular dichroism and (c) Zeta potential comparison of mSP, DNA encapsulated mSP (mSP-DNA), and pDNA. (d) Electromobility shift assay (EMSA). mSP-DNA has lower mobility than free pDNA. mSPs protect DNA from

degradation by DNase I. (e) Elemental analysis of mSP-DNA (i) An SEM image of mSP-DNA (ii-v) Elemental analysis of the mSPs and location of iron, sulfur, oxygen, and phosphorus (DNA specific signal) elements in mSP-DNA. (vi) overlay image of four elements. DNA is localized in the center of mSPs. (f) Graph shows relative DNA release percentage during acid incubation time of mSP-pDNA for 48h. (g) Red box zoomed graph shows DNA release percentage for 2h. (h) Gel electrophoresis shows free DNA after 30 min acid incubation along with intact mSP-pDNA.

Author Manuscript

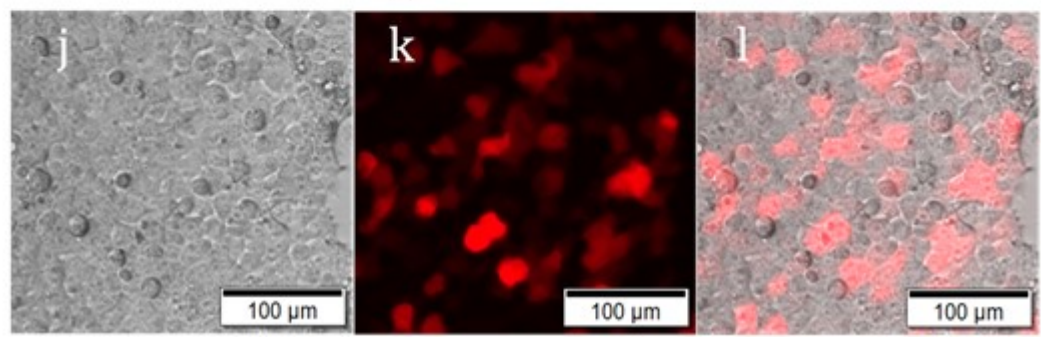
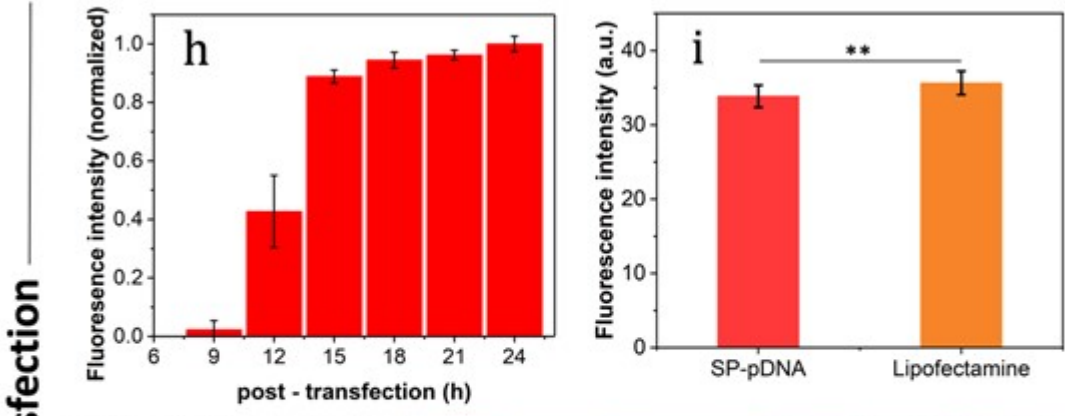
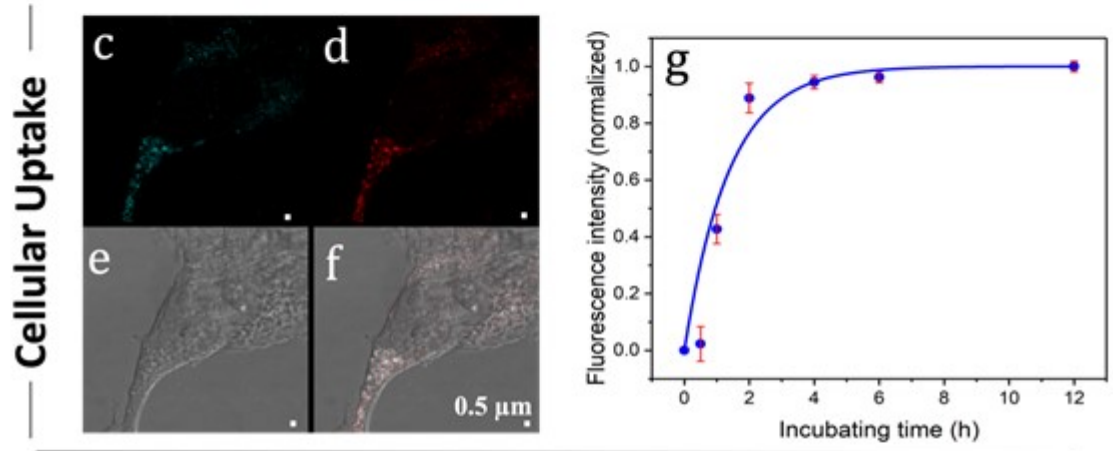
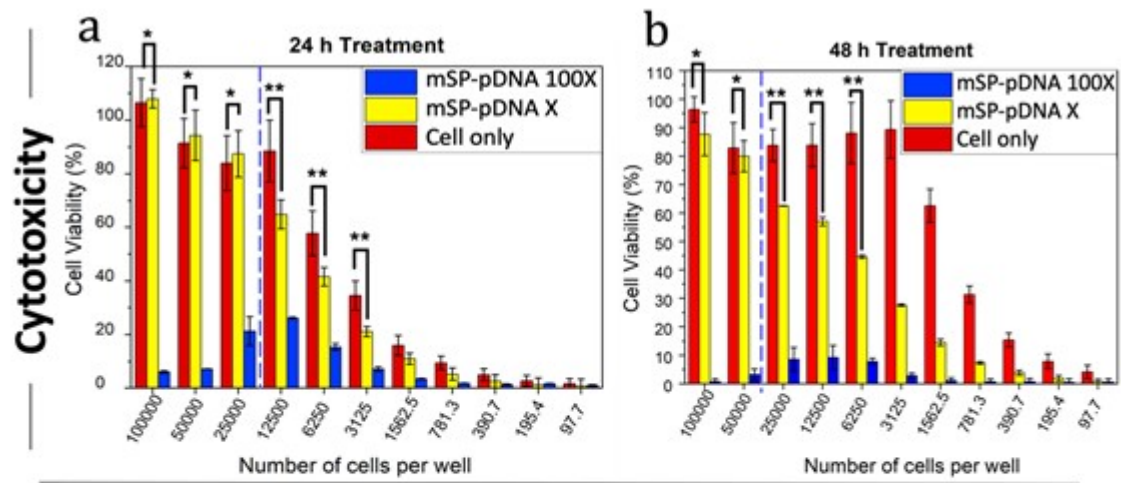


Figure 6: Cytotoxicity, cellular uptake, and transfection data. (a-b) Cell viability assay for mSP-DNA X and 100X along with cell only for (a) 24h treatment and (b) 48h treatment. Dashed lines show the threshold of cell: particle ratio for significant cell viability reduction. *p-value* * <0.05, ** >0.05. (c-f) A confocal image of cellular uptake of mSP after 12h. mSP in the cell in (c) is excited at 475 nm, and in (d) is excited at 500 nm; the emission window for both excitations is 520-570nm. (f) mSP aggregations can be seen in a cell. (g) Average fluorescence intensity of confocal images of mSP treated cells. (h-l) Transfection capability of mSP-DNA analysis, (h) Average fluorescence intensity of confocal images of mSP-DNA treated cells post-transfection 6-24h. At 24 h, it reaches the highest transfections efficiency. (i) Comparative evaluation of transfection efficiency by mSPs and lipofectamine. (j-l) Confocal images of cells post-transfection 24h. mCherry protein gives a red color to the cells. Scale bars: (c-f) 0.5 μ m, (j-l)100 μ m

Author Manuscript

Thermostability

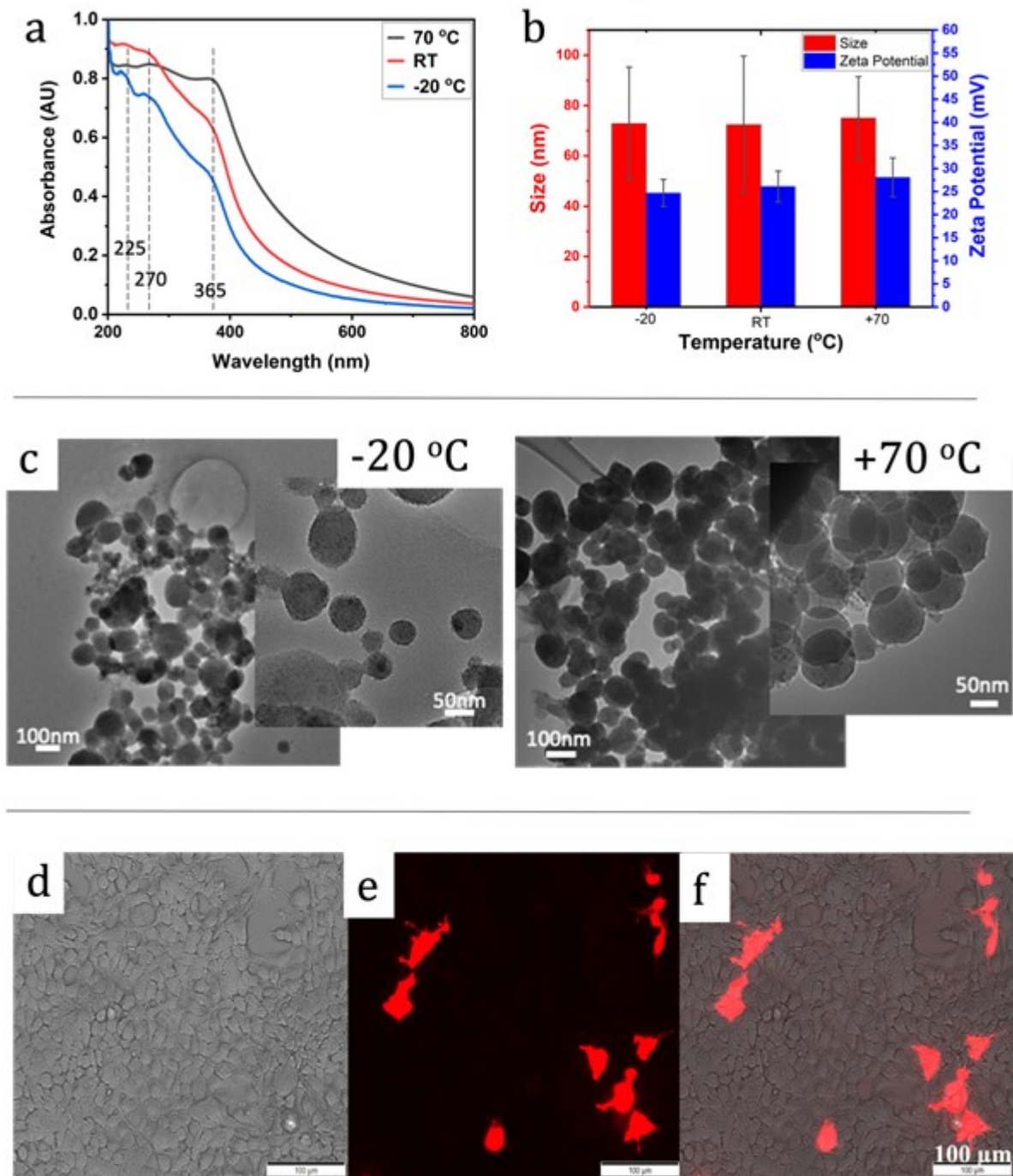


Figure 7: Thermostability data of SP. (a) UV-Vis spectrum of SP that is kept at -20 °C for 6 years, room temperature (RT) for 4 years, and 70 °C for 50 hours. (b) TEM size and zeta potential data of the same set in (a), red color shows the size, and blue shows zeta potential (c) TEM images of SPs after keeping them at -20 and +70 for >4 years. (d-f) Confocal images of cells post-transfection 24h with SP-DNA that is kept at 70 °C for 48h. mCherry protein gives a red color to the cells. Scale bar: 100μm

Reference

1. Bayoumi, M., Bayley, H., Maglia, G. & Sapa, K. T. Multi-compartment encapsulation of communicating droplets and droplet networks in hydrogel as a model for artificial cells. *Sci. Rep.* **7**, 1–11 (2017).
2. Kushner, D. J. Self-assembly of biological structures. *Bacteriol. Rev.* **33**, 302–45 (1969).
3. Yang, M., Chan, H., Zhao, G., Bahng, J. H. J. H., Zhang, P., Král, P. & Kotov, N. A. N. A. Self-assembly of nanoparticles into biomimetic capsid-like nanoshells. *Nat Chem* **9**, 287–294 (2017).
4. Mitragotri, S. & Lahann, J. Physical approaches to biomaterial design. *Nat. Mater.* **8**, 15–23 (2009).
5. Kerfeld, C. A., Heinhorst, S. & Cannon, G. C. Bacterial Microcompartments. *Annu. Rev. Microbiol.* **64**, 391–408 (2010).
6. Kerfeld, C. A., Sawaya, M. R., Tanaka, S., Nguyen, C. V, Phillips, M., Beeby, M. & Yeates, T. O. Protein Structures Forming the Shell of Primitive Bacterial Organelles. *Science (80-.).* **309**, 936–938 (2005).
7. Yeates, T. O., Kerfeld, C. A., Heinhorst, S., Cannon, G. C. & Shively, J. M. Protein-based organelles in bacteria: carboxysomes and related microcompartments. *Nat. Rev. Microbiol.* **6**, 681–691 (2008).
8. Settembre, C., Fraldi, A., Medina, D. L. & Ballabio, A. Signals from the lysosome: a control centre for cellular clearance and energy metabolism. *Nat. Rev. Mol. Cell Biol.* **14**, 283–96 (2013).
9. Tanaka, S., Kerfeld, C. A., Sawaya, M. R., Cai, F., Heinhorst, S., Cannon, G. C. & Yeates, T.

- O. Atomic-level models of the bacterial carboxysome shell. *Science* (80-.). **319**, 1083–1086 (2008).
10. Martin, W. Evolutionary origins of metabolic compartmentalization in eukaryotes. *Philos. Trans. R. Soc. B Biol. Sci.* **365**, 847–855 (2010).
 11. Zhu, H., Fan, J., Du, J. & Peng, X. Fluorescent Probes for Sensing and Imaging within Specific Cellular Organelles. *Acc. Chem. Res.* **49**, 2115–2126 (2016).
 12. Lentini, R., Yeh Martín, N. & Mansy, S. S. Communicating artificial cells. *Current Opinion in Chemical Biology* vol. 34 53–61 at <https://doi.org/10.1016/j.cbpa.2016.06.013> (2016).
 13. Voeltz, G. K., Rolls, M. M. & Rapoport, T. A. Structural organization of the endoplasmic reticulum. *EMBO Rep.* **3**, 944–950 (2002).
 14. Chen, A. H. & Silver, P. A. Designing biological compartmentalization. *Trends Cell Biol.* **22**, 662–70 (2012).
 15. Tawfik, D. S. & Griffiths, A. D. Man-made cell-like compartments for molecular evolution. *Nat. Biotechnol.* **16**, 652–656 (1998).
 16. Zhu, T. F. & Szostak, J. W. Coupled Growth and Division of Model protocell membranes. *J. Am. Chem. Soc.* **131**, 5705–5713 (2009).
 17. Balakumaran, A., Pawelczyk, E., Ren, J., Sworder, B., Chaudhry, A., Sabatino, M., Stroncek, D., Frank, J. A. & Robey, P. G. Superparamagnetic iron oxide nanoparticles labeling of bone marrow stromal (mesenchymal) cells does not affect their ‘stemness’. *PLoS One* **5**, e11462 (2010).
 18. CHANNON, K., BROMLEY, E. & WOOLFSON, D. Synthetic biology through biomolecular design and engineering. *Curr. Opin. Struct. Biol.* **18**, 491–498 (2008).

19. Belluati, A., Thamboo, S., Najer, A., Maffei, V., Planta, C., Craciun, I., Palivan, C. G. & Meier, W. Multicompartment Polymer Vesicles with Artificial Organelles for Signal-Triggered Cascade Reactions Including Cytoskeleton Formation. *Adv. Funct. Mater.* 2002949 (2020) doi:10.1002/adfm.202002949.
20. Aldaye, F. A., Palmer, A. L. & Sleiman, H. F. Assembling Materials with DNA as the Guide. *Science* (80-.). **321**, 1795–1799 (2008).
21. Wei, B., Dai, M. & Yin, P. Complex shapes self-assembled from single-stranded DNA tiles. *Nature* **485**, 623–626 (2012).
22. Paleos, C. M., Tsiourvas, D., Sideratou, Z. & Pantos, A. Formation of artificial multicompartment vesosome and dendrosome as prospected drug and gene delivery carriers. *Journal of Controlled Release* vol. 170 141–152 at <https://doi.org/10.1016/j.jconrel.2013.05.011> (2013).
23. Bolinger, P.-Y., Stamou, D. & Vogel, H. An Integrated Self-Assembled Nanofluidic System for Controlled Biological Chemistries. *Angew. Chemie* **120**, 5626–5631 (2008).
24. Peters, R. J. R. W., Marguet, M., Marais, S., Fraaije, M. W., van Hest, J. C. M. & Lecommandoux, S. Cascade reactions in multicompartmentalized polymersomes. *Angew. Chemie* **53**, 146–50 (2014).
25. Marguet, M., Edembe, L. & Lecommandoux, S. Polymersomes in polymersomes: Multiple loading and permeability control. *Angew. Chemie - Int. Ed.* **51**, 1173–1176 (2012).
26. Godoy-Gallardo, M., Labay, C., Trikalitis, V. D., Kempen, P. J., Larsen, J. B., Andresen, T. L. & Hosta-Rigau, L. Multicompartment Artificial Organelles Conducting Enzymatic Cascade Reactions inside Cells. *ACS Appl. Mater. Interfaces* **9**, 15907–15921 (2017).
27. Hosta-Rigau, L., York-Duran, M. J., Zhang, Y., Goldie, K. N. & Städler, B. Confined multiple

- enzymatic (cascade) reactions within poly(dopamine)-based capsosomes. *ACS Appl. Mater. Interfaces* **6**, 12771–12779 (2014).
28. Chandrawati, R., Odermatt, P. D., Chong, S. F., Price, A. D., Städler, B. & Caruso, F. Triggered cargo release by encapsulated enzymatic catalysis in capsosomes. *Nano Lett.* **11**, 4958–4963 (2011).
29. Engelhart, A. E., Adamala, K. P. & Szostak, J. W. A simple physical mechanism enables homeostasis in primitive cells. *Nat. Chem.* **8**, 448–453 (2016).
30. Huang, Y., Xiao, A., Hou, G., Li, H., Chen, P., Chen, C. & Guan, B.-O. Impact of MoS₂ supporting interface on the photothermal-induced deformation of gold nanoshells: tracked through an optical microfiber. *2D Mater.* (2019) doi:10.1088/2053-1583/ab2c22.
31. Khalid, M., Ciraci, C., Khalid, M. & Ciraci, C. Numerical Analysis of Nonlocal Optical Response of Metallic Nanoshells. *Photonics* **6**, 39 (2019).
32. Liu, Y. F., Wang, Y. Q., Liu, Y. F. & Wang, Y. Q. Thermo-Electro-Mechanical Vibrations of Porous Functionally Graded Piezoelectric Nanoshells. *Nanomaterials* **9**, 301 (2019).
33. Pampalakis, G. From Chemical Gardens to Quasibiological Inorganic Cells. *ChemistrySelect* **4**, 2802–2805 (2019).
34. Barge, L. M., Cardoso, S. S. S., Cartwright, J. H. E., Cooper, G. J. T., Cronin, L., De Wit, A., Doloboff, I. J., Escribano, B., Goldstein, R. E., Haudin, F., Jones, D. E. H., Mackay, A. L., Maselko, J., Pagano, J. J., Pantaleone, J., Russell, M. J., Sainz-Díaz, C. I., Steinbock, O., Stone, D. A., Tanimoto, Y. & Thomas, N. L. From Chemical Gardens to Chemobrionics. *Chem. Rev.* **115**, 8652–8703 (2015).
35. Wang, J., Zhu, B., Wang, Y., Hao, Y., Zhang, J. & Li, Z. Polymer pattern-induced self-

- assembly of inorganic nanoparticles. *Soft Matter* **18**, 97–106 (2021).
36. Xu, F., Zhang, P., Navrotsky, A., Yuan, Z. Y., Ren, T. Z., Halasa, M. & Su, B. L. Hierarchically assembled porous ZnO nanoparticles: Synthesis, surface energy, and photocatalytic activity. *Chem. Mater.* **19**, 5680–5686 (2007).
 37. Yi, C., Yang, Y., Liu, B., He, J. & Nie, Z. Polymer-guided assembly of inorganic nanoparticles. *Chem. Soc. Rev.* **49**, 465–508 (2020).
 38. Caruso, F., Spasova, M., Susha, A., Giersig, M. & Caruso, R. A. Magnetic nanocomposite particles and hollow spheres constructed by a sequential layering approach. *Chem. Mater.* **13**, 109–116 (2001).
 39. Iskandar, F., Mikrajuddin & Okuyama, K. In Situ Production of Spherical Silica Particles Containing Self-Organized Mesopores. *Nano Lett.* **1**, 231–234 (2001).
 40. Walsh, D., Lebeau, B. & Mann, S. Morphosynthesis of Calcium Carbonate (Vaterite) Microsponges. *Adv. Mater.* **11**, 324–328 (1999).
 41. Jung, J. H., Ono, Y. & Shinkai, S. Novel preparation method for multi-layered, tubular silica using an azacrown-appended cholesterol as template and metal-deposition into the interlayer space. *J. Chem. Soc. Perkin Trans. 2* **0**, 1289–1291 (1999).
 42. Ono, Y., Kanekiyo, Y., Inoue, K., Hojo, J., Nango, M. & Shinkai, S. Preparation of novel hollow fiber silica using collagen fibers as a template. *Chem. Lett.* 475–476 (1999) doi:10.1246/cl.1999.475.
 43. Van Bommel, K. J. C., Friggeri, A. & Shinkai, S. Organic templates for the generation of inorganic materials. *Angewandte Chemie - International Edition* vol. 42 980–999 at <https://doi.org/10.1002/anie.200390284> (2003).

44. Raee, E., Sun, X., Yang, Y., Xu, X., Zhou, Y., Sahai, N. & Liu, T. Electrostatic interaction regulated self-assembly of simple inorganic macroions into blackberry structures and their possible role as compartment systems in the origin of life. *Giant* **12**, 100125 (2022).
45. Kotov, N. A. Inorganic Nanoparticles as Protein Mimics. *Science* **330**, 188–189 (2010).
46. Glotzer, S. C. & Solomon, M. J. Anisotropy of building blocks and their assembly into complex structures. *Nat. Mater.* **6**, 557–562 (2007).
47. Tang, Z., Kotov, N. A. & Giersig, M. Spontaneous Organization of Single CdTe Nanoparticles into Luminescent Nanowires. *Science (80-.)*. **297**, 237–240 (2002).
48. Ariga, K., Hill, J. P., Lee, M. V, Vinu, A., Charvet, R. & Acharya, S. Challenges and breakthroughs in recent research on self-assembly. *Sci. Technol. Adv. Mater.* **9**, 014109 (2008).
49. Kotov, N. A. Practical aspects of self-organization of nanoparticles: Experimental guide and future applications. *J. Mater. Chem.* **21**, (2011).
50. De Yoreo, J. J., Gilbert, P. U. P. A. P. A., Sommerdijk, N. A. J. M. J. M., Penn, R. L., Whitelam, S., Joester, D., Zhang, H., Rimer, J. D., Navrotsky, A., Banfield, J. F., Wallace, A. F., Michel, F. M., Meldrum, F. C., Cölfen, H. & Dove, P. M. Crystallization by particle attachment in synthetic, biogenic, and geologic environments. *Science (80-.)*. **349**, aaa6760 (2015).
51. Tang, L., Vo, T., Fan, X., Vecchio, D., Ma, T., Lu, J., Hou, H., Glotzer, S. C. & Kotov, N. A. Self-Assembly Mechanism of Complex Corrugated Particles. *J. Am. Chem. Soc.* **143**, 19655–19667 (2021).
52. Qu, Z., Feng, W.-J., Wang, Y., Romanenko, F. & Kotov, N. A. Diverse nanoassemblies of graphene quantum dots and their mineralogical counterparts. *Angew. Chemie* **59**, 8542–8551

- (2020).
53. Lee, S., Sim, K., Moon, S. Y., Choi, J., Jeon, Y., Nam, J.-M., Park, S.-J., Lee, S., Moon, S. Y., Choi, J., Jeon, Y., Park, S.-J., Sim, K. & Nam, J.-M. Controlled Assembly of Plasmonic Nanoparticles: From Static to Dynamic Nanostructures. *Adv. Mater.* **33**, 2007668 (2021).
 54. Gao, M. R., Zhang, S. R., Jiang, J., Zheng, Y. R., Tao, D. Q. & Yu, S. H. One-pot synthesis of hierarchical magnetite nanochain assemblies with complex building units and their application for water treatment. *J. Mater. Chem.* **21**, 16888–16892 (2011).
 55. Tang, Z., Zhang, Z., Wang, Y., Glotzer, S. C. & Kotov, N. A. Self-assembly of CdTe nanocrystals into free-floating sheets. *Science* **314**, 274–8 (2006).
 56. Shevchenko, E. V, Talapin, D. V, Murray, C. B., O'Brien, S., Elena V. Shevchenko, *, Dmitri V. Talapin, †, Christopher B. Murray, *, A. & O'Brien‡, S. Structural characterization of self-assembled multifunctional binary nanoparticle superlattices. *J. Am. Chem. Soc.* **128**, 3620–37 (2006).
 57. Srivastava, S., Santos, A., Critchley, K., Kim, K.-S. S., Podsiadlo, P., Sun, K., Lee, J., Xu, C., Lilly, G. D., Glotzer, S. C. & Kotov, N. A. Light-controlled self-assembly of semiconductor nanoparticles into twisted ribbons. *Science (80-)*. **327**, 1355–9 (2010).
 58. Xia, Y., Nguyen, T. D., Yang, M., Lee, B., Santos, A., Podsiadlo, P., Tang, Z., Glotzer, S. C. & Kotov, N. A. Self-assembly of self-limiting monodisperse supraparticles from polydisperse nanoparticles. *Nat. Nanotechnol.* **6**, 580–587 (2011).
 59. Feng, W., Kim, J.-Y. Y., Wang, X., Calcaterra, H. A., Qu, Z., Meshi, L. & Kotov, N. A. Assembly of mesoscale helices with near-unity enantiomeric excess and light-matter interactions for chiral semiconductors. *Sci. Adv.* **3**, e1601159 (2017).
 60. Yang, M. & Kotov, N. A. Nanoscale helices from inorganic materials. *J. Mater. Chem.* **21**,

- 6775–6792 (2011).
61. Yan, J., Feng, W., Kim, J. Y., Lu, J., Kumar, P., Mu, Z., Wu, X., Mao, X. & Kotov, N. A. Self-Assembly of Chiral Nanoparticles into Semiconductor Helices with Tunable near-Infrared Optical Activity. *Chem. Mater.* **32**, 476–488 (2020).
 62. Zhou, H., Kim, J.-P., Bahng, J. H., Kotov, N. A. & Lee, J. Self-Assembly Mechanism of Spiky Magnetoplasmonic Supraparticles. *Adv. Funct. Mater.* **24**, 1439–1448 (2014).
 63. Wei, A., Kasama, T. & Dunin-Borkowski, R. E. Self-assembly and flux closure studies of magnetic nanoparticle rings. *J. Mater. Chem.* **21**, 16686–16693 (2011).
 64. de Q. Silveira, G., Ramesar, N. S., Nguyen, T. D., Bahng, J. H., Glotzer, S. C. & Kotov, N. A. Supraparticle Nanoassemblies with Enzymes. *Chem. Mater.* **31**, (2019).
 65. Park, J. Il, Nguyen, T. D., de Queirós Silveira, G., Bahng, J. H., Srivastava, S., Zhao, G., Sun, K., Zhang, P., Glotzer, S. C. & Kotov, N. a. Terminal supraparticle assemblies from similarly charged protein molecules and nanoparticles. *Nat. Commun.* **5**, 3593 (2014).
 66. Xia, Y. & Tang, Z. Monodisperse inorganic supraparticles: formation mechanism, properties and applications. *Chem. Commun. (Camb)*. **48**, 6320–6336 (2012).
 67. Zhou, Y., Marson, R. L., van Anders, G., Zhu, J., Ma, G., Ercius, P., Sun, K., Yeom, B., Glotzer, S. C. & Kotov, N. A. Biomimetic Hierarchical Assembly of Helical Supraparticles from Chiral Nanoparticles. *ACS Nano* 3248–56 (2016) doi:10.1021/acsnano.5b05983.
 68. Piccinini, E., Pallarola, D., Battaglini, F. & Azzaroni, O. Self-limited self-assembly of nanoparticles into supraparticles: towards supramolecular colloidal materials by design. *Mol. Syst. Des. Eng.* **1**, 155–162 (2016).
 69. Zhao, L., Song, X., Ouyang, X., Zhou, J., Li, J. & Deng, D. Bioinspired Virus-like

- Fe₃O₄/Au@C Nanovector for Programmable Drug Delivery via Hierarchical Targeting. *ACS Appl. Mater. Interfaces* **13**, 49631–49641 (2021).
70. Lawson, R. T. R. T. Aqueous Oxidation of Pyrite by Molecular Oxygen. *Chem. Rev.* **82**, 461–497 (1982).
71. Bai, Y., Yeom, J., Yang, M., Cha, S. H., Sun, K. & Kotov, N. a. Universal synthesis of single-phase pyrite FeS₂ nanoparticles, nanowires, and nanosheets. *J. Phys. Chem. C* **117**, 2567–2573 (2013).
72. Chen, G., Zhu, Z. & Qin, Y. Synthesis of Pure Micro- and Nanopyrite and Their Application for As (III) Removal from Aqueous Solution. *Adv. Mater. Sci. Eng.* **2016**, 1–6 (2016).
73. Holder, C. F. & Schaak, R. E. Tutorial on Powder X-ray Diffraction for Characterizing Nanoscale Materials. *ACS Nano* **13**, 7359–7365 (2019).
74. Ou, C. R., Shen, C. I. & Ou, C. M. Biocompatibility of Fe₂O₃ nanoparticles for the activation of Glia cell migration. *J. Supercond. Nov. Magn.* **23**, 1197–1199 (2010).
75. Alam, T., Khan, R. A. A., Ali, A., Sher, H., Ullah, Z. & Ali, M. Biogenic synthesis of iron oxide nanoparticles via *Skimmia laureola* and their antibacterial efficacy against bacterial wilt pathogen *Ralstonia solanacearum*. *Mater. Sci. Eng. C. Mater. Biol. Appl.* **98**, 101–108 (2019).
76. Liu, W., Kappl, M. & Butt, H. J. Tuning the Porosity of Supraparticles. *ACS Nano* **13**, 13949–13956 (2019).
77. Jafari, S., Derakhshankhah, H., Alaei, L., Fattahi, A., Varnamkhasti, B. S. & Saboury, A. A. Mesoporous silica nanoparticles for therapeutic/diagnostic applications. *Biomed. Pharmacother.* **109**, 1100–1111 (2019).
78. Liu, Y., Ye, W., Lin, H., Song, C., Rong, Z., Lu, R., Zhang, H., Huang, H., Tang, Z. & Zhang,

- S. Embedding Pd-Cu Alloy Nanoparticles in Shell of Surface-Porous N-Doped Carbon Nanosphere for Selective Hydrogenation of p-Chloronitrobenzene. *Chinese J. Chem.* **39**, 2843–2851 (2021).
79. Tang, Y., Varyambath, A., Ding, Y., Chen, B., Huang, X., Zhang, Y., Yu, D. G., Kim, I. & Song, W. Porous organic polymers for drug delivery: hierarchical pore structures, variable morphologies, and biological properties. *Biomater. Sci.* **10**, 5369–5390 (2022).
80. Ennaoui, A., Fiechter, S., Goslowsky, H. & Tributsch, H. Photoactive Synthetic Polycrystalline Pyrite (FeS₂). *J. Electrochem. Soc.* **132**, 1579–1582 (1985).
81. Ennaoui, A., Fiechter, S., Jaegermann, W. & Tributsch, H. Photoelectrochemistry of Highly Quantum Efficient Single-Crystalline n-FeS₂ (Pyrite). *J. Electrochem. Soc.* **133**, 97 (1986).
82. Zangeneh Kamali, K., Alagarsamy, P., Huang, N. M., Ong, B. H. & Lim, H. N. Hematite Nanoparticles-Modified Electrode Based Electrochemical Sensing Platform for Dopamine. *Sci. World J.* **2014**, 1–13 (2014).
83. Kwon, J., Jun, S. W., Choi, S. I., Mao, X., Kim, J., Koh, E. K., Kim, Y.-H., Kim, S.-K., Hwang, D. Y., Kim, C.-S. & Lee, J. FeSe quantum dots for in vivo multiphoton biomedical imaging. *Sci. Adv.* **5**, eaay0044 (2019).
84. Murugan, N., Prakash, M., Jayakumar, M., Sundaramurthy, A. & Sundramoorthy, A. K. Green synthesis of fluorescent carbon quantum dots from *Eleusine coracana* and their application as a fluorescence ‘turn-off’ sensor probe for selective detection of Cu²⁺. *Appl. Surf. Sci.* **476**, 468–480 (2019).
85. Ali, M., Anjum, A. S., Riaz, R., Bibi, A., Sun, K. C. & Jeong, S. H. Unraveling the surface states related Stokes shift dependent electrocatalytic activity of N-doped carbon quantum dots

- for photovoltaic applications. *Carbon N. Y.* **181**, 155–168 (2021).
86. Kotov, N. A. *Nanoparticle assemblies and superstructures*. (Dekker/CRC Press, 2006).
87. Wu, Z., Liu, J., Li, Y., Cheng, Z., Li, T., Zhang, H., Lu, Z. & Yang, B. Self-Assembly of Nanoclusters into Mono-, Few-, and Multilayered Sheets via Dipole-Induced Asymmetric van der Waals Attraction. *ACS Nano* **9**, 6315–23 (2015).
88. Hirai, K., Yeom, B., Chang, S.-H. S., Chi, H., Mansfield, J. F., Lee, B., Lee, S., Uher, C. & Kotov, N. A. Coordination Assembly of Discoid Nanoparticles. *Angew. Chemie Int. Ed.* **54**, 8966–8970 (2015).
89. Batista, C. A. S., Larson, R. G., Kotov, N. A., Silvera Batista, C. A., Larson, R. G. & Kotov, N. A. Nonadditivity of nanoparticle interactions. *Science (80-.)*. **350**, 1242477–1242477 (2015).
90. Deng, K., Luo, Z., Tan, L. & Quan, Z. Self-assembly of anisotropic nanoparticles into functional superstructures. *Chem. Soc. Rev.* **49**, 6002–6038 (2020).
91. Tang, Z., Zhang, Z., Wang, Y., Glotzer, S. C. & Kotov, N. A. Self-assembly of CdTe nanocrystals into free-floating sheets. *Science (80-.)*. **314**, (2006).
92. Jiang, W., Qu, Z. B., Kumar, P., Vecchio, D., Wang, Y., Ma, Y., Bahng, J. H., Bernardino, K., Gomes, W. R., Colombari, F. M., Lozada-Blanco, A., Veksler, M., Marino, E., Simon, A., Murray, C., Muniz, S. R., Moura, A. F. de, Kotov, N. A., de Moura, A. F., Kotov, N. A., Moura, A. F. de & Kotov, N. A. Emergence of complexity in hierarchically organized chiral particles. *Science (80-.)*. **368**, 642–648 (2020).
93. Randić, M. & Plavšić, D. On the concept of molecular complexity. *Croat. Chem. Acta* **75**, 107–116 (2002).

94. Lošdorfer Božič, A., Šiber, A. & Podgornik, R. Statistical analysis of sizes and shapes of virus capsids and their resulting elastic properties. *J. Biol. Phys.* **39**, 215–28 (2013).
95. Lidmar, J., Mirny, L. & Nelson, D. R. Virus shapes and buckling transitions in spherical shells. *Phys. Rev. E Stat. Nonlin. Soft Matter Phys.* **68**, 051910 (2003).
96. Ghosh, S., Brown, A. M., Jenkins, C. & Campbell, K. Viral Vector Systems for Gene Therapy: A Comprehensive Literature Review of Progress and Biosafety Challenges. *Appl. Biosaf.* **25**, 7–18 (2020).
97. Porterfield, J. Z. & Zlotnick, A. A Simple and General Method for Determining the Protein and Nucleic Acid Content of Viruses by UV Absorbance. *Virology* **407**, 281 (2010).
98. Kostrikis, L. G., Liu, D. J. & Day, L. A. Ultraviolet Absorbance and Circular Dichroism of Pfl Virus: Nucleotide/Subunit Ratio of Unity, Hyperchromic Tyrosines and DNA Bases, and High Helicity in the Subunits*’*. *Biochemistry* **33**, 1694–1703 (1994).
99. Nasir, N. & Al Ahmad, M. Cells Electrical Characterization: Dielectric Properties, Mixture, and Modeling Theories. *J. Eng. (United Kingdom)* **2020**, (2020).
100. Simeonova, M., Wachner, D. & Gimsa, J. Cellular absorption of electric field energy: Influence of molecular properties of the cytoplasm. *Bioelectrochemistry* **56**, 215–218 (2002).
101. Peng, S., Zeng, Q., Yang, X., Hu, J., Qiu, X. & He, J. Local Dielectric Property Detection of the Interface between Nanoparticle and Polymer in Nanocomposite Dielectrics. *Sci. Reports* **2016 6**, 1–9 (2016).
102. Zhang, N. N., Li, X. F., Deng, Y. Q., Zhao, H., Huang, Y. J., Yang, G., Huang, W. J., Gao, P., Zhou, C., Zhang, R. R., Guo, Y., Sun, S. H., Fan, H., Zu, S. L., Chen, Q., He, Q., Cao, T. S., Huang, X. Y., Qiu, H. Y., Nie, J. H., Jiang, Y., Yan, H. Y., Ye, Q., Zhong, X., Xue, X. L., Zha, Z. Y., Zhou, D., Yang, X., Wang, Y. C., Ying, B. & Qin, C. F. A Thermostable mRNA

- Vaccine against COVID-19. *Cell* **182**, 1271-1283.e16 (2020).
103. Sahin, U., Muik, A., Vogler, I., Derhovanessian, E., Kranz, L. M., Vormehr, M., Quandt, J., Bidmon, N., Ulges, A., Baum, A., Pascal, K. E., Maurus, D., Brachtendorf, S., Lörks, V., Sikorski, J., Koch, P., Hilker, R., Becker, D., Eller, A. K., Grützner, J., Tonigold, M., Boesler, C., Rosenbaum, C., Heesen, L., Kühnle, M. C., Poran, A., Dong, J. Z., Luxemburger, U., Kemmer-Brück, A., Langer, D., Bexon, M., Bolte, S., Palanche, T., Schultz, A., Baumann, S., Mahiny, A. J., Boros, G., Reinholz, J., Szabó, G. T., Karikó, K., Shi, P. Y., Fontes-Garfias, C., Perez, J. L., Cutler, M., Cooper, D., Kyratsous, C. A., Dormitzer, P. R., Jansen, K. U. & Türeci, Ö. BNT162b2 vaccine induces neutralizing antibodies and poly-specific T cells in humans. *Nat.* 2021 5957868 **595**, 572–577 (2021).
104. Jackson, L. A., Anderson, E. J., Roupael, N. G., Roberts, P. C., Makhene, M., Coler, R. N., McCullough, M. P., Chappell, J. D., Denison, M. R., Stevens, L. J., Pruijssers, A. J., McDermott, A., Flach, B., Doria-Rose, N. A., Corbett, K. S., Morabito, K. M., O'Dell, S., Schmidt, S. D., Swanson, P. A., Padilla, M., Mascola, J. R., Neuzil, K. M., Bennett, H., Sun, W., Peters, E., Makowski, M., Albert, J., Cross, K., Buchanan, W., Pikaart-Tautges, R., Ledgerwood, J. E., Graham, B. S. & Beigel, J. H. An mRNA Vaccine against SARS-CoV-2 — Preliminary Report. *N. Engl. J. Med.* **383**, 1920–1931 (2020).
105. Youn, H. & Chung, J. K. Modified mRNA as an alternative to plasmid DNA (pDNA) for transcript replacement and vaccination therapy. <http://dx.doi.org/10.1517/14712598.2015.1057563> **15**, 1337–1348 (2015).
106. Schlake, T., Thess, A., Fotin-Mleczek, M. & Kallen, K.-J. Developing mRNA-vaccine technologies. *RNA Biol.* **9**, 1319–30 (2012).
107. Karikó, K., Buckstein, M., Ni, H. & Weissman, D. Suppression of RNA Recognition by Toll-like Receptors: The Impact of Nucleoside Modification and the Evolutionary Origin of RNA.

Immunity **23**, 165–175 (2005).

108. Krennsner, P. G., Mann, P., Kroidl, A., Leroux-Roels, I., Schindler, C., Gabor, J. J., Schunk, M., Leroux-Roels, G., Bosch, J. J., Fendel, R., Kreidenweiss, A., Velavan, T. P., Fotin-Mleczek, M., Mueller, S. O., Quintini, G., Schönborn-Kellenberger, O., Vahrenhorst, D., Verstraeten, T., Alves de Mesquita, M., Walz, L., Wolz, O. O., Oostvogels, L., De Boever, F., Desimpel, A., Esen, M., Fischer, I., Flügge, J., Geisenberger, O., Geldmacher, C., Held, K., Hoffmann, L., Hölscher, M., Huber, K., Jacobs, B., Joye, J., Kirschke, J., Klopp, N., Koehne, E., Köhler, C., Lalremruata, A., Lamsfus-Calle, C., Linh, L. T. K., Maes, C., Metaxa, D., Molnar, M. L., Mueller, M., Müller-Schöner, G., Quindel, M., Rappe, S., Schultze-Naumburg, L., Schumacher, C., Schuster, S., Thiel, V., Vejda, S., Waerlop, G., Westenberg, C., Wons, K. & Zeder, A. Safety and immunogenicity of an mRNA-lipid nanoparticle vaccine candidate against SARS-CoV-2: A phase 1 randomized clinical trial. *Wien. Klin. Wochenschr.* **133**, 931–941 (2021).

FeS₂ NPs self-assemble into biomimetic supraparticles with multiple interconnected compartments. High complexity of the particles manifests in their functionality. They successfully encapsulate nucleic acid cargo, deliver it inside the cells and protect it against degradation in the environment.